2-1-2016

Novel light trapping techniques for silicon solar cells.

Ahmed Emad Khalifa

The American University in Cairo

School of Science and Engineering

Novel Light Trapping Techniques for Silicon Solar Cells

A Thesis Submitted to

The Department of Nanotechnology

In Partial Fulfillment of the Requirements for

The Degree of Master of Science

By

Ahmed Emad ElDean ElSayed Khalifa

June 2016

The American University in Cairo

School of Science and Engineering

Novel Light Trapping Techniques for Silicon Solar Cells

By
Ahmed E. Khalifa

Submitted to
The Department of Nanotechnology
In Partial Fulfillment of the requirements for
The Degree of Master of Science

Dr. Mohamed Swillam(Advisor) Assistant Professor and Associate Chair, Physics Department, AUC	Date
Dr. Joumana ElRifai (Internal examiner) Assistant Professor, Physics Department, AUC	Date
Dr. Khalid Kirah (External Examiner) Professor, Engineering Physics Department, Ain Shams Univ.	Date
Dr. Karim Addas (Moderator) Associate Professor and Director, Physics Graduate Program, Physics Department, AUC	Date

Contents

LIST OF FIGURES

LIST OF ABBREVIATIONS

AFM Atomic force microscopy

AM1.5 Air mass 1.5 solar irradiance

a-Si:H Hydrogenated amorphous silicon

nc-Si:H/μc-Si:H Hydrogenated nanocrystalline/microcrystalline silicon

CVD chemical vapor deposition

EQE External quantum efficiency

FF Fill factor

ITO Indium tin oxide

J_{sc} Short-circuit current density

n Refractive index

SEM Scanning electron microscopy

TCO Transparent conductive oxide

*V*oc Open-circuit voltage

ZnO / ZnO:Al Zinc oxide / Aluminium-doped zinc oxide

ACKNOWLEDGMENTS

I would like to express my gratitude to my thesis Supervisor, Dr. Mohamed Swillam, for giving me the opportunity to work in his research group and for guiding me through the work. Dr. Mohamed, through both the courses he teaches and through my thesis supervision, has added a lot to my knowledge related to many photonics/Nanophotonics topics even beyond the scope of the thesis.

My gratitude also goes to Dr. Hamdy Abd Elhamid in the Center Of Nanoelectronics and Devices (CND) in Zewail City of Science and Technology for guiding me on the electrical simulation part and providing me with many resources to use and understand the simulation tools.

I would also like to thank many faculty members, especially Dr. Nageh Allam for the energy conversion materials course and other fruitful scientific discussions.

I would also like to thank many members of the Nanophotonics research supervised by Dr. Swillam. Before mentioning particular names, I would like to thank all members for the fruitful discussions and experience sharing. I would like to thank AbdelAziz for the collaboration in the silicon nanocones part and Mohamed Elsayed for helping in measurements and SEM images.

Last but not least I would like to express my appreciation for my family and friends for their love and encouragement.

ABSTRACT

Thin-film silicon photovoltaic (PV) solar cells have attracted significant interest for decades due to the increasing demand for clean and sustainable energy resources. Further reduction of the cost of materials and manufacturing processes is required to reach the grid parity where the cost of electricity from solar PV cells is equal to the cost of other nonrenewable resources. Crystalline and thin-film silicon solar cells are anticipated to continue to be one of the dominant solar PV cell technologies. This anticipation is due to the abundance of silicon and the successful history of a continuous drop in cost in silicon-based PV cells.

In this thesis, several designs were investigated to enhance absorption of sunlight in the active layers of silicon-based solar cells. In the first design, a plasmonic enhancement to silicon solar cells using (Titanium nitride) TiN as a replacement for silver is studied. In the second, a new design for tandem thin-film silicon solar cells is proposed using a periodic layer between the two subcells. Finally, a low-cost easily fabricated nanocone facial textures is proposed and showed promising experimental and simulation antireflection properties.

3D electromagnetic analysis was performed using finite difference time domain (FDTD) simulations to all structures and 3D Device simulations were additionally used to study the tandem cell structure. These contributions which were published are believed to contribute towards achieving high efficiency and cost-effective solar cells.

1 INTRODUCTION

1.1 Overview and potential of solar energy

Different forms of fossil fuels remain the main source of electrical energy in the world. Even with the most optimistic views, the current reserve will deplete sooner or later. In addition to the limitedness of reserves, those sources pose very bad effect on the climate and the environment. One of the promising solutions is utilizing the solar energy, through different means as will be explained, to produce clean and renewable energy sources.

Solar energy is one of the energy sources that are capable of replacing all non-renewable sources. With a total power of 120,000 TW hitting the earth surface, the total world energy consumption in one year is less than the amount of solar energy reaching the earth's surface in one hour [1,2]. The total capacity of all other renewable resources like geothermal, Wind, Biomass and Hydropower altogether can't fulfill the future world energy needs in the following decades. With this great potential, cost-effective ways to produce energy from the sun is the topic of numerous research endeavors.

Solar energy has two basic means to be converted into electrical energy. The first is using Solar thermal energy to heat water, produce steam and drive a turbine, the second is direct conversion of sunlight into electricity using the photovoltaic effect.

The amount of solar energy (solar irradiance) incident on the outermost Earth's atmospheric layers is almost constant; however, the radiation at the Earth's surface varies widely due to absorption and scattering of the atmosphere, clouds, pollution, latitude, season of the year and of course the time of day.

The solar irradiance has been measured and standardized in various conditions. To reflect the effect of the atmosphere on the amount of solar irradiation, Air mass (AM) convention is used. AM0 represents the solar irradiance outside the atmosphere and AM1.5 is the irradiation when the location has a zenith angle (angle between line normal to the surface and sun) of around 48 degrees. It is now standard practice to measure solar cell performance at AM1.5G

solar irradiance (where G stands for global and accounts for direct and diffused incident irradiance) [3]. The AM1.5G is expressed in Watts per m^2 per nm as shown in Figure 1-1 . It can be deduced from the same figure that the total power is around $1000W/m^2$, where around 9% is in the ultraviolet range, 39% in the visible and 52% in the infrared.

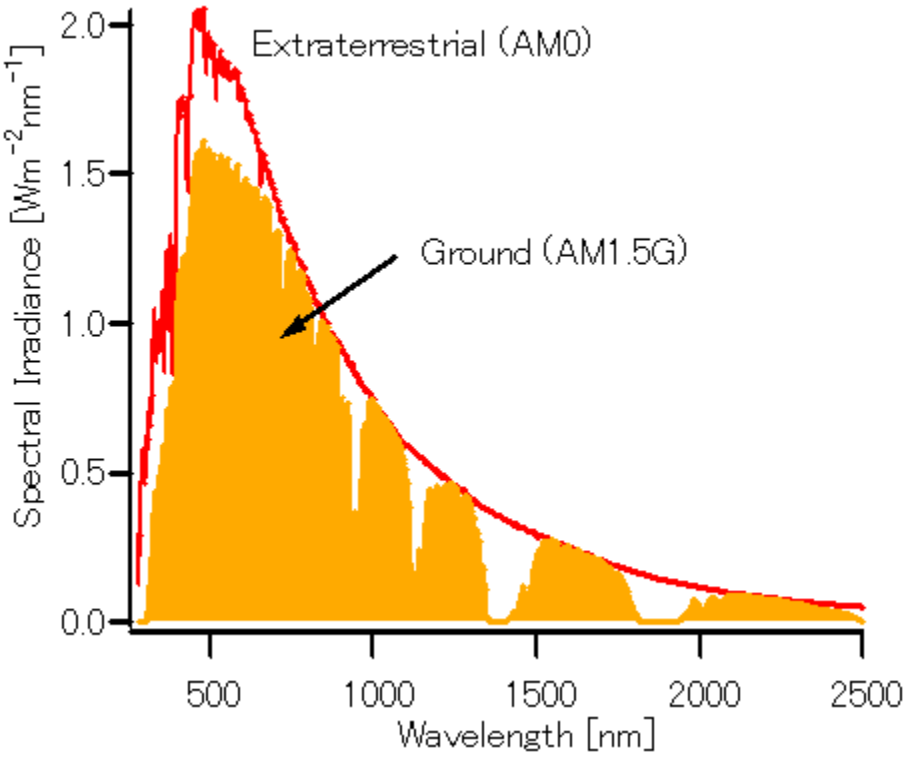

Figure 1-1 Solar irradiance spectra. AM0 and AM1.5G is shown. Figure from (https://commons.wikimedia.org/wiki/File:SunLightSpectrum-280-2500nm.PNG)

Using the famous E=hv equation, where E is the energy of a photon, h is Planck constant and v is the frequency of the photon, the number of photons/sec incident on a m^2 at each wavelength in the solar irradiance can be calculated. This amount is called photon flux.

1.2 Photovoltaics and its different realizations

The thesis addresses thin-film silicon Photovoltaic cells specifically, as opposed to other solar energy harvesting techniques like thermal methods. In general Photovoltaics (PV) or solar cells are devices that convert sunlight into direct current (DC) electricity. Cells are electrically connected in parallel and/or series into modules and arrays, the DC current can then charge batteries or drive electrical loads usually after being converted to Alternating current (AC) to power conventional electrical loads. These PV systems can act as standalone systems, or can be connected alongside the electrical grid.

The Photovoltaic effect was discovered in the nineteenth century while the basic photovoltaic cell was realized in Bell Labs in 1957 using silicon PN junctions. From that date, a lot of materials and techniques have been used in photovoltaic cells, while still monocrystalline silicon solar cells are the dominant technology. Examples of notable materials and techniques are CdS, GaAS, amorphous silicon, polycrystalline silicon, nanocrystalline silicon, Dyesensitized solar cells, organic solar cells and many others [3,4].

Photovoltaic cells have progressed significantly in both efficiency and cost. Single junction solar cells with a record efficiency of 28.8% and multi-junction cells with efficiency (under concentrated light) of 44.4% have been realized and confirmed independently [5]. The research community is still trying hard to achieve better cost effective cells using cheaper materials, or by using cheaper fabrications processes.

Photovoltaic cells are generally categorized into three generations. In the first generation, mono or multi-crystalline silicon or III-V semiconductor alloys are the absorbers. The second generation utilizes thin-film substances deposited on flexible substrates and provides cheaper PV cells with lower efficiency, examples are CIGS (Copper-Indium-Gallium-Selenide), CdTe (Cadmium-Telluride), and amorphous silicon in addition to organic and dyesensitized cells. The third generation using new concepts like quantum dots, up-down converters, hot carriers, multiple e-h pair excitations and plasmonic structures is anticipated to combine the best of the first two generations(efficiency and low cost)[4,6].

Traditional photovoltaic cells operate basically using three steps. First, electron in the light absorbing material (active layer), get excited by photons having energy greater than the material bandgap, the result is a free electron-hole (e-h) pair. Second, a selective mechanism, for example the built-in field of a PN junction, causes the free electrons to move in one direction (cathode) and the holes in another direction (anode). Third and last, the free electrons travel in an outer circuitry, release some energy in the electric load and then return to the cathode to combine with holes and return the absorber into ground state.[3]

Bandgap of the active layer is one of the most important parameters that the active absorber layer is chosen based on. If the bandgap (E_g) has a small energy value, all photons with energy greater than this value can be absorbed; however, the difference in energy between photons and the bandgap will be eventually released and lost (thermalization loss). On the contrary, if the bandgap has high energy value, only high energy photons can be absorbed, and the rest of the sun irradiance will be wasted (Figure 1-2).

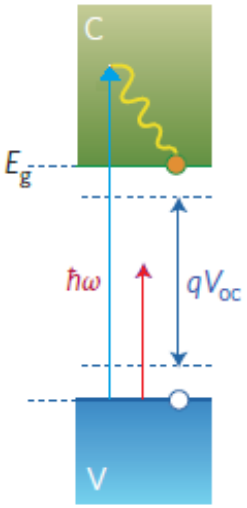

Figure 1-2, Interaction between sunlight photons and absorber material: energy diagram of the absorber layer. Photon ħω (blue arrow) with energy larger than the bandgap excites an electron from the valence (V) to the conduction (C) band of the absorber. After thermalization, an electron–hole pair is formed across the bandgap with energy E_g. Photons with energy below the bandgap (red arrow) are not absorbed. The open circuit voltage V_{oc} is lower than the bandgap (E_g) due to entropic reasons [7]. Permission to reproduce figure was granted by Nature publishing group.

Efficiency limits of solar cells have been studied from the early 60's by Shockley and Queisser[8] and the limit is known after their names by Shockley–Queisser limit. Using fundamental physical laws, the limit calculates solar conversion efficiency to be around 33% assuming a single p-n junction with an absorber that has a band gap of 1.34 eV. It is worth noting that the most used solar cell material, silicon, has a close band gap of 1.1 eV.

The ultimate maximum solar cell efficiency is usually calculated by the thermodynamic limit as the Shockley–Queisser limit applies only to cells with a single p-n junction. Cells with multiple absorber layers having different bandgaps already exceed this limit as indicated before. Several other studies have been conducted and the limit is in the 80s% range [6,7].

1.3 Thin-film silicon solar cells (TFSSC)

1.3.1 Overview

Silicon has many properties that make it currently (and possibly for decades to come) the dominant solar cell active absorber layer. As for a certain absorber to constitute the active part of solar cells and provide the TWs of power the world needs, it must be abundant and relatively cheap among other properties like good electrical properties. Silicon is the second most abundant element in the earth upper crust [9], although it is worth noting that it doesn't exist in the pure form.

Crystalline silicon (c-Si) is used widely in the electronics industry and still is the dominant technology of solar cell industry for decades. They are grown as rods using Czochralski or Float Zone energy intensive methods and subsequently cut into wafers of various sizes and thicknesses (normally hundreds of micrometers) depending on the application.

Lately amorphous and nanocrystalline silicon are used in many industries including solar cells. One of their main advantages is that they can be deposited using relatively low temperature (~250 C) plasma enhanced chemical vapor deposition (PECVD). The structure of the atoms in both materials is not ordered, has voids and in turn has bad electrical properties. The gases used for deposition are Silane or Disilane (SiH_4 or Si_2H_6). Alloying can be done with

materials, like germanium, carbon to increase or decrease the bandgap and doping can be done with traditional materials like phosphorous and boron but in their gas form.

One of the main enhancements to their electric properties is using hydrogen in the PECVD process. Hydrogen atoms help passivates the silicon atoms and In the case of nanocrystalline silicon has an additional role when the dilution ratio of hydrogen gases with respect to Silane or Disilane gases are high enough. This high dilution rate causes nucleation of silicon and forms the nano crystals of the nc-Si (see Figure 1-3). The result of introducing hydrogen is hydrogenated a-Si (aSi: H) and hydrogenated nc-Si (nc-Si:H)[4].

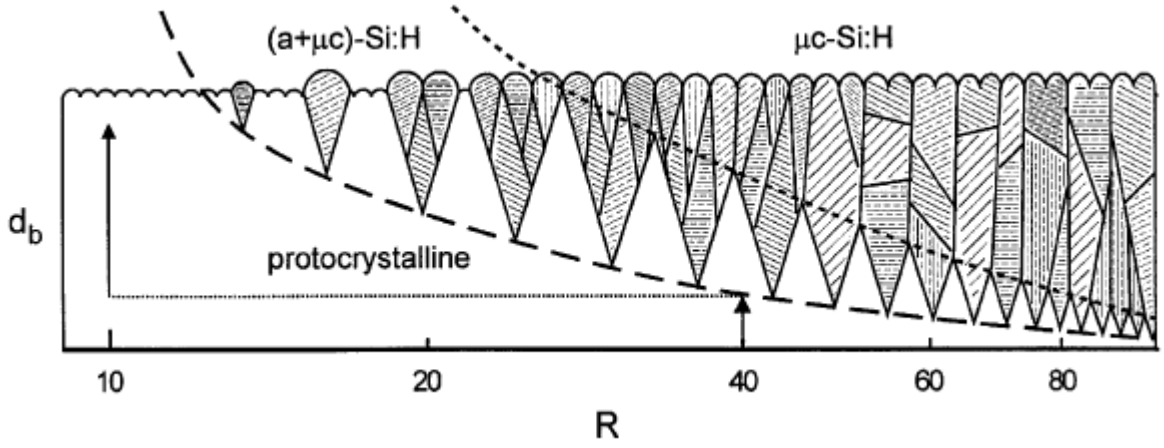

Figure 1-3, Effect of H dilution of silane (dilution ratio $R=H_2/SiH_4$). The dashed and dotted lines identify the a-(a+nc),and(a+ nc)-nc transitions, respectively[10].Permission to reproduce the figure was granted by Elsevier.

One of the main serious concerns with a-Si:H is the Light induced degradation (LID or sometimes named after its discoverers as Staebler–Wronski effect), where extended exposure to light decreases the photoconductivity and dark conductivity of a-Si : H. It is worth noting that Annealing above 150 °C reverses the process [11]. . It is also known that the effect is reduced when the layer is thinner and that make a thickness constraint on the design of a-Si:H cells . As for nc-Si, it shows growing level of LID depending on its amorphous content.

Although widely studied, until now there is no agreement in the exact mechanism of LID[12,13]. The degradation is mainly caused by photo creation of dangling bonds, although

silicon-silicon bonds, silicon-hydrogen bonds and hydrogen roles in the process are investigated [12].

Studying the absorption coefficients of a-Si and nc-Si and comparing it to the c-Si, one can deduce several things (see Figure 1-4). First, a-Si and nc-Si (μc-Si in Figure and the two terms are used interchangeably in literature) have better values in the short wavelengths and this can be attributed to their disordered atomic arrangement. Second, their overlapping values suggest the use of more than one of them in tandem cells as will be shown later.

One of the worth noting cells using more than one form of silicon is silicon heterojunction technology (Si-HJT). These solar cells comprise nanometers-thin amorphous silicon layers on monocrystalline silicon wafers. In addition to the clever use of bandgaps, the key point of these structures is the shift of high recombination contacts from the crystalline surface by addition of the a-Si intrinsic and doped layers. Efficiency of large-area cells (~140 cm^2) of 25.6% has been reported by Panasonic which is the current world record of silicon-based solar cells [5].

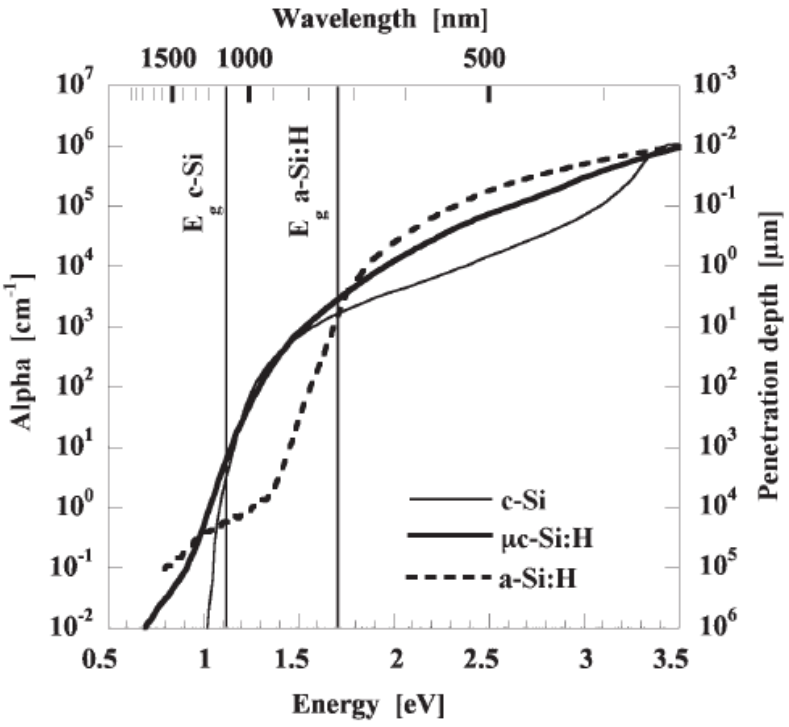

Figure 1-4, absorption coefficients (Alpha) and its reciprocal (penetration depth) of c-Si, nc-Si (μc-Si) and a-Si[14]. Permission to reproduce this figure was granted by John Wiley & Sons.

1.3.2 Cell Structure

TFSSCs have different structures than c-Si cells, as their electrical properties such as diffusion length and mobility for both electrons and holes in a-Si:H or nc:Si are smaller than their c-Si counterpart. Doped a-Si:H layers have even more defect states than intrinsic silicon thin-film layers. P-i-n junctions are used instead of PN junctions and that is to build high electric field to drive generated carriers towards the terminals. In summary, TFSSC are drift based, while c-Si cells are diffusion based [3,4].

TFSSC whether made of a-Si or nc-Si are categorized into two main types, n-i-p and p-i-n. Figure 1-5 shows n-i-p (substrate) and p-i-n (superstrate) devices where main difference is the order of deposition. In the n-i-p structure, the n-doped layer is the first silicon layer to be deposited on the back contact, while in the p-i-n structure; it is the p-doped layer which is initially deposited on the front contact [4,15].

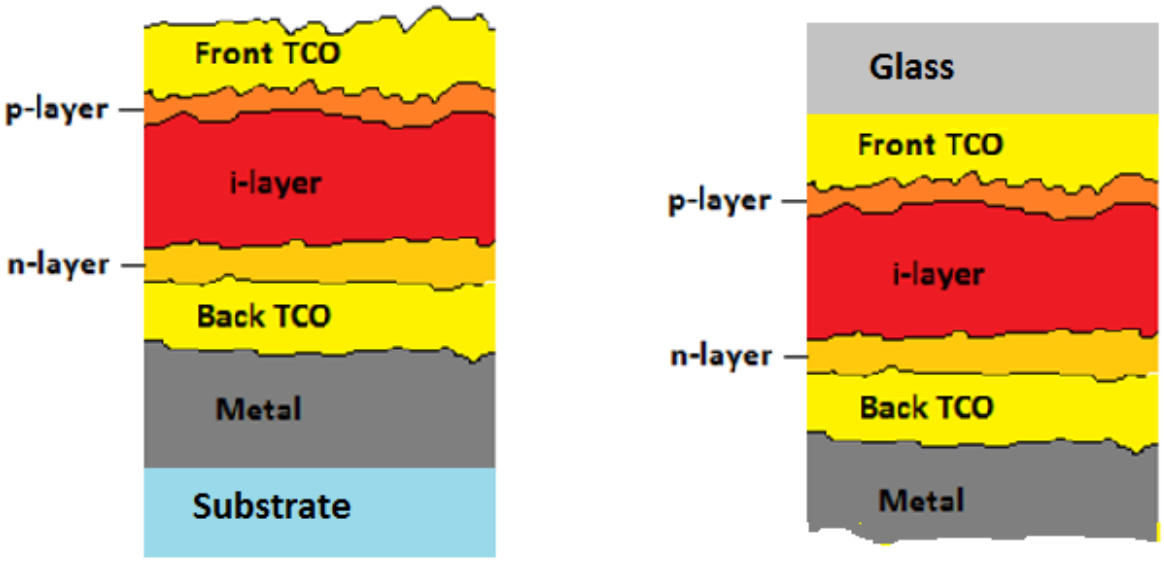

Figure 1-5 , left figure shows nip (substrate) and right shows pin (superstrate) configuration of a-Si cells. Nc-Si cells have exactly same configuration, the main difference is that the i-layer are usually much thicker (~1-3 um).

In addition to the n,i and p silicon layers, the TFSSC usually contains I-glass, II-front transparent conductive oxide (TCO) for collecting holes and light trapping, III-back TCO for acting as diffusion barrier layer and also for light trapping and IV-metal(can be replaced partially

by a dielectric reflector) for collecting electrons and reflecting light. It is worth noting that the doped p and n layers don't contribute to carrier generation due to their defection and hence are usually much thinner.

More complex structures are used now as the current record efficiency of the above cells is less than 12% [5]. Double or triple junction cells configurations has better efficiency. One of the famous structures are Micromorph (microcrystalline and amorphous cells connected in series) cells shown in Figure 1-6. In the micromorph cells, top a-Si:H cell absorbs light with wavelengths up to around 750-800 nm while the nc-Si:H bottom cell can absorb light in the near infrared region.

In addition to the previously mentioned advantages, TFSSC has good temperature coefficient that make them suitable for warm countries and a lot of research has to be done to increase their efficiency and further enhance our manufacturing process.

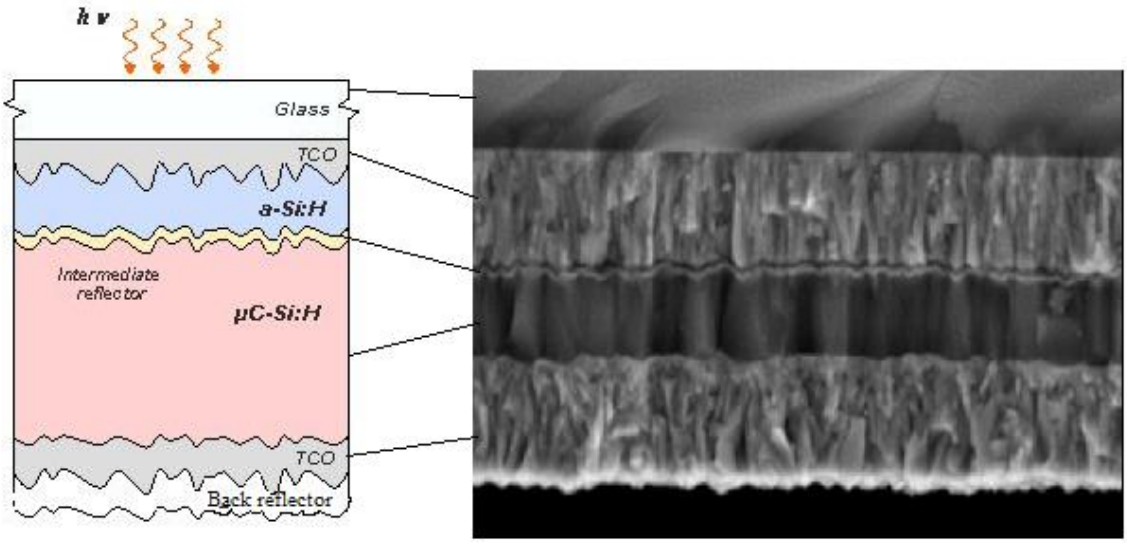

Figure 1-6, left part shows schematic and right part shows SEM image of a micromorph superstrate tandem cell. (adopted from http://pvlab.epfl.ch/thin_film_on_glass). Thickness of a-Si:H cell is 250nm, IRL 200nm and nc-Si is 1.5um. Reproduction of this figure was granted by pvlab.

1.4 JV, generation rate and EQE

Output power per unit, P_{out}, can be calculated as the product of J and V, where J is the current density, usually measured in mA/cm^2 and V is the output voltage. A typical JV curve of the solar cell is shown in Figure 1-7. Short circuit current density, J_{sc}, is one of the important specifications and is defined as the current produced by the cell under illumination and when device is short circuited. On the other hand, open circuit voltage, V_{oc} is the voltage when the cell is open circuited. The maximum power that the device can produce is at the largest product of the JV curve.

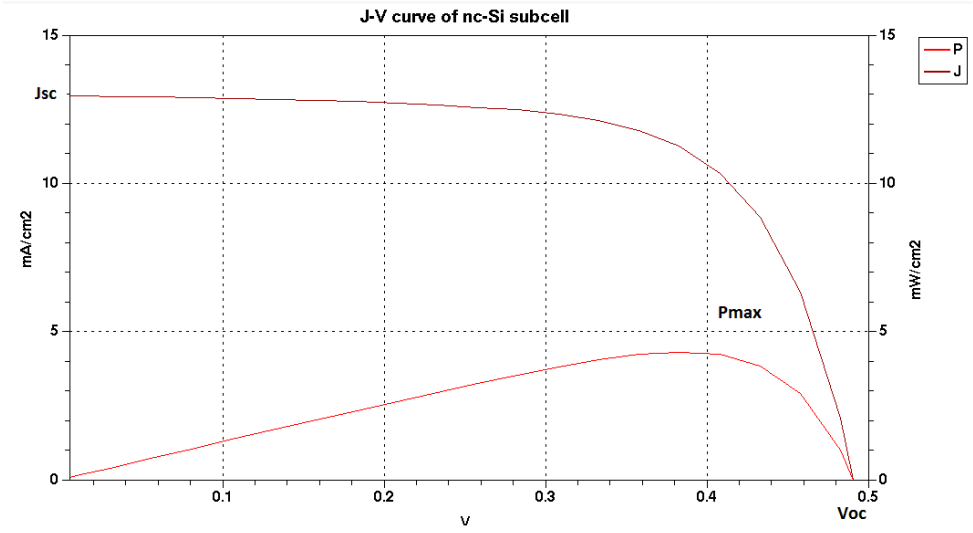

Figure 1-7, showing a current density-voltage (J-V) of a nc-Si subcell in a micromorph cell under illumination. The short-circuit current density J_{sc} and open-circuit voltage V_{oc} are displayed. The maximum power point (MPP) is the largest JV product in the curve (P_{max}).

Hence, efficiency of the solar cell can be calculated as

$$\eta = \frac{J_{mp}V_{mp}}{P_{in}} \qquad (1.1)$$

Where J_{mp} and V_{mp} are values of J and V at the maximum power point and Pin is the input solar power and can calculated by integrating the solar irradiance, discussed before in section 1.1, over the range of wavelengths that the cell absorbs.

In an ideal solar cell, the J_{sc} would be the same from 0V to V_{oc} and to measure the deviation from this ideal behavior a new value called fill factor (FF) was defined. FF, always less than one, is the ratio of the maximum power to the product of V_{oc} and J_{sc}.

External Quantum efficiency ($EQE(\lambda)$) is the ratio of the number of photo-generated electron-hole pairs rate per unit area (Generation rate G(λ)) to the rate of incident photons per unit area (flux) at a particular wavelength. Ideally, $EQE(\lambda)$ would be one for wavelength smaller than that of the bandgap and zero for wavelengths smaller than the bandgap. However, in real solar cell, part of the light is reflected back or absorbed in non-active layers and this makes the $\mathrm{EQE}(\lambda)$ values less than one. The short circuit current Jsc can be calculated from:

$$Jsc = e \int EQE(\lambda).\phi_{AM\ 1.5}(\lambda) d\,\lambda = \frac{e}{h.c} \int \lambda . EQE(\lambda). I_{AM\ 1.5}(\lambda) d\,\lambda \qquad (1.2)$$

Where e, h, and c are the electron charge, Planck's constant and speed of light respectively, while ϕ and I are the AM1.5 photon flux and solar irradiance respectively. The above equation is derived from multiplying the electron charge by the number of electrons excited per second per unit area. At each wavelength the photon flux multiplied by EQE gives the number of photon absorbed per second per unit area and integrating the multiplication over the wavelength absorption range of the material calculates the number of photons (and hence electrons excited) per second per unit area. The above analysis ignores any recombination effects and assumes 100% collection efficiency of charge carriers. Hence, it can be more accurately called photo-generated current density.

1.5 Scope and Outline of the thesis

The main goal of the thesis is studying and suggesting novel light trapping structures, the the thesis is organized as follows:

Chapter 1: is a basic introduction to the PVs terminologies and how PV cells work.

Chapter 2 : is a literature review of different light management techniques.

Chapter 3: is an overview of the optoelectronic simulation techniques.

Chapter 4: has two parts. First plasmonic TiN based designs are investigated and second, a new intermediate reflector layer is proposed and studied numerically.

Chapter 5 demonstrates experimental and simulation studies of low-cost lithography-free nanotexturing of monocrystalline silicon.

Chapter 6 is the conclusion and future work.

2 LITERATURE REVIEW OF LIGHT MANAGEMENT IN SILICON SOLAR CELLS

Light management is important in all types of all solar cells including crystalline silicon solar cells; however, it is more important in TFSSC and other types that have electrical constraints on the active layer thickness. Light management techniques can be categorized into three main types: 1) Minimizing reflection and parasitic losses. 2) Light trapping and scattering. 3) Efficient use of sun irradiance [4].

2.1 Minimizing reflection and parasitic losses.

Reflection due to optical refractive index mismatch between the cell and upper media is one of the oldest identified optical losses in solar cells. This problem is solved by adding one or more antireflection coatings and/or using textured surfaces.

Antireflection coatings (ARC) with materials that have both almost-zero extinction coefficient at the wavelengths of interest and a refractive index with a value between that of air and silicon are used for decades on monocrystalline solar cells. Si_3N_4, MgF_2 and SiO_2 are among the most famous materials. It is worth nothing that these upper ARC layer can play an important role in passivating the front surface of the silicon wafer and hence enhancing the electrical efficiency of the cell[16].

ARC coatings can be single or multi layered of different materials. Main concept of the ARC coating is the induced destructive interference between the reflected wave at the ARC/air interface and the ARC/silicon interface causing the total two reflected waves to be zero at a specific wavelength (see Figure 2-1). Only one wavelength has zero or minimal reflectance in the whole AM1.5 spectrum and it can be chosen to be in the visible light wavelength range where the solar irradiance is at its maximum. Using multilayer ARCs enable achieving a better anti-reflection performance across the whole wavelength range.[17]

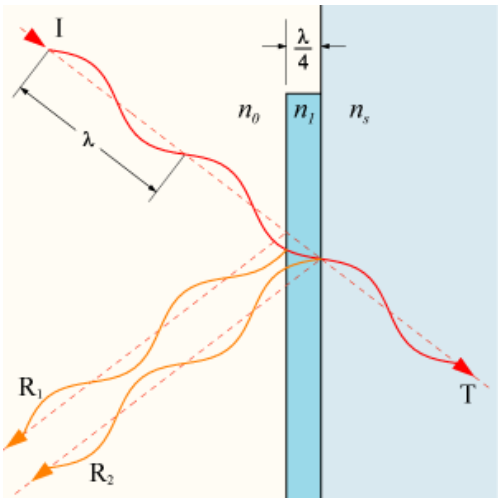

Figure 2-1, showing basic anti-reflection coating with thickness equal to quarter the wavelength to achieve zero surface reflection at a specific wavelength[18].

For crystalline silicon solar cells, many materials are used as ARCs, including SiO2(n=1.46), Si_3N_4(n=2.05), TiO_2(n=2.62), SiO_x(n=1.8-1.9), MgF_2(n=1.38), ZnS(n=2.36) and Al_2O_3(n=1.76)[17].

Antireflection coatings in TFSSC sometimes play the additional role of aiding in charge collection like the case of nip solar cells, where front(facing the sun) TCO, for example indium-doped tin-oxide (ITO), has thickness adjusted to satisfy anti-reflection in addition to electrical conductance requirements.

Surface texturing is also utilized from many decades to minimize monocrystalline silicon reflection. Using basic ray optics analysis, it can be easily shown that the incident light waves will reflect back and forth between inclined surfaces with each time a fraction of incident power is transmitted into the cell (see Figure 2-2).

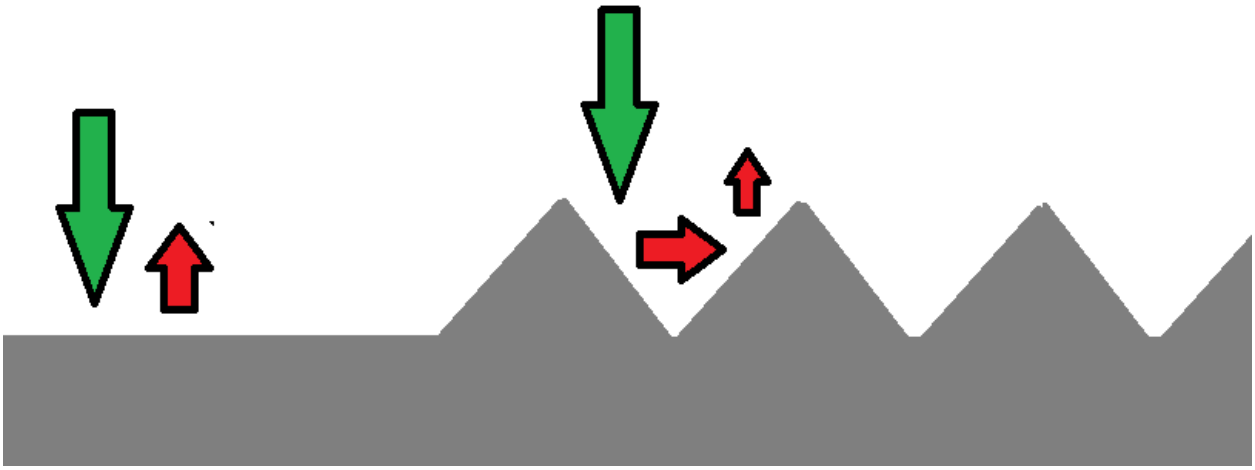

Figure 2-2, illustrating how texturing can minimize the overall reflection of silicon as shown in the right side of the schematic relative to flat surface as shown in the left side (width of arrows indicate intensity of light)

Basic texturing can be done in relatively simple and cost efficient techniques in monocrystalline solar cells. Using chemical wet etching with an alkaline is one of the simplest ways and can produce ideal periodic pyramid shapes in case of monocrystalline silicon. In each different crystalline face and direction, the atoms are organized in a different way, so the strength between the atoms is different and will respond differently to chemical solutions.

The {100} planes in silicon have the lowest density of silicon atoms, hence minimum covalent bonds and high etching rates while the {111} planes is the opposite. That's the principle of "Anisotropic wet etching" that occurs in the Si crystalline wafers and are used to build pyramidal textures in solar cells (see Figure 2-3).

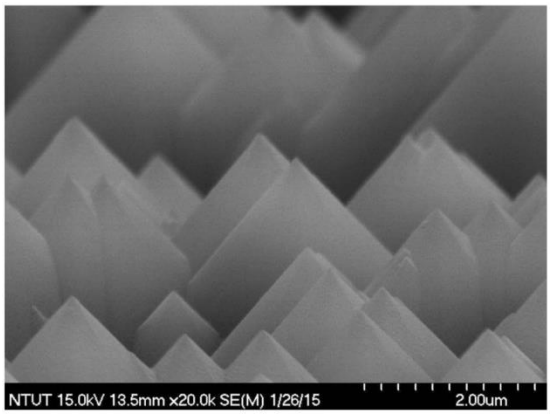

Figure 2-3, SEM of a pyramid textured silicon surface[19]. Permission to reuse was granted by creative commons license of the MDPI publisher.

One of the highly efficient textures for crystalline silicon cells is the inverted pyramids shape although the fabrication involves lithography, laser or other techniques. Although, recently researchers produced same inverted with low-cost by maskless Cu-nanoparticles assisted etching in Cu(NO3)2 / HF / H2O2 / H2O solution[20].

Textured surfaces can be used solely or with antireflection coatings to provide a broadband reflection minimization layer, in addition to scattering passed light and providing long optical paths for photons inside the cell.

In addition to ARCs and texturing, lossless reflection in the backside of the cell is needed to reflect back the unabsorbed light. The famous PERL silicon solar cell (Passivated Emitter Rear Locally Diffused, see Figure 2-4) which originated from University of New South Wales in Australia[21] and held the best efficiency record for more than 10 years uses all of the above techniques with inverted pyramids as the chosen texturing method in addition to a thin back SiO2 layer (according to the reputable NREL National center for photovoltaics (http://www.nrel.gov/ncpv/) efficiency chart. Also the recent sunpower cell which currently holds the highest efficiency record uses both ARC and texturing simultaneously in addition to moving all electrodes to the backside.

The optical features of the above-mentioned sunpower cell is as follows: a) The front side is textured with random pyramids (54.75°) and coated with a passivating SiO_2 film and an anti-reflective film(Specifics of the ARC material couldn't be found); the texture refracts the incident light so that it travels with angles to the plane of the cell, thus increasing the optical thickness. b) The rear surface is coated with SiO_2 except for metal contacts, were both negative and positive electrodes form a pattern of interdigitated fingers over the cell.

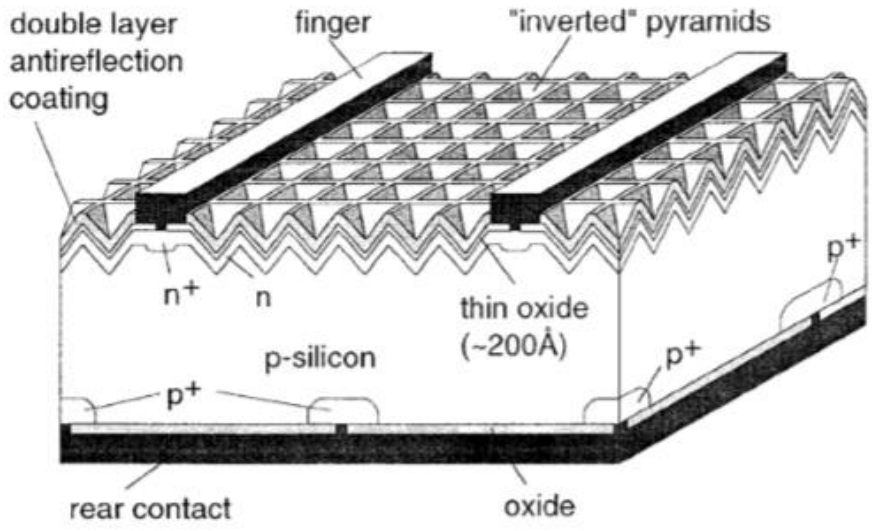

Figure 2-4, High efficiency PERL cell were inverted pyramids textures of oxides is used[21]. Permission to reproduce this figure was granted by John Wiley and Sons.

In multicrystalline silicon based cells were there is no contiguous crystal planes exist, photolithographic techniques and lasers as well as mechanically sculpting can be used.

As can be easily expected, requirements of ARCs and texturing of amorphous, nanocrystalline or micromorph cells are complicated due to its very thin active layers. While simple optics rules and ray tracing can be used to study textures and ARCs in crystalline cells, they can't be directly applied to the above mentioned types of cells. Requirements can be summarized[22] as a) strong light scattering into large angle for entire absorption wavelength range, b) suitable smooth substrate features to guarantee a high quality of the deposited silicon c) balancing conduction and transparency of front electrodes which also acts as ARCs.

Parasitic losses in layers not contributing to electrical output of the cell is also an area where enhancements are needed. New doped materials with large bandgaps such as hydrogenated amorphous/microcrystalline silicon carbide (a-SiC:H/μc-SiC:H) and hydrogenated amorphous/microcrystalline silicon oxide (a-SiO_x:H/μc-SiO_x:H) are now used to minimize losses in doped layers[23,24]. For the same reasons, other back reflectors such as dielectric ones or photonic crystals are being investigated instead of the lossy metal layers [25,26].

2.2 Light trapping and scattering.

The ultimate goal of light trapping in solar cells is to keep all photons in the active layer until being absorbed. Once the light enters the active part of the cell, Light scattering of front textures and back surface reflection and scattering lengthen the path the photon takes and hence increase the "optical thickness" of the material. In other words, increasing the path length is attributed to the scattered path the photon takes in addition to the total internal reflection at the active layer interfaces.

The scattering effects in the thin non-crystalline silicon cells are often studied by using what is called the haze factor which is the ratio of diffused transmission over total transmission(diffused and specular)[27]. Different optical paths for incident light are shown in Figure 2-5 below.

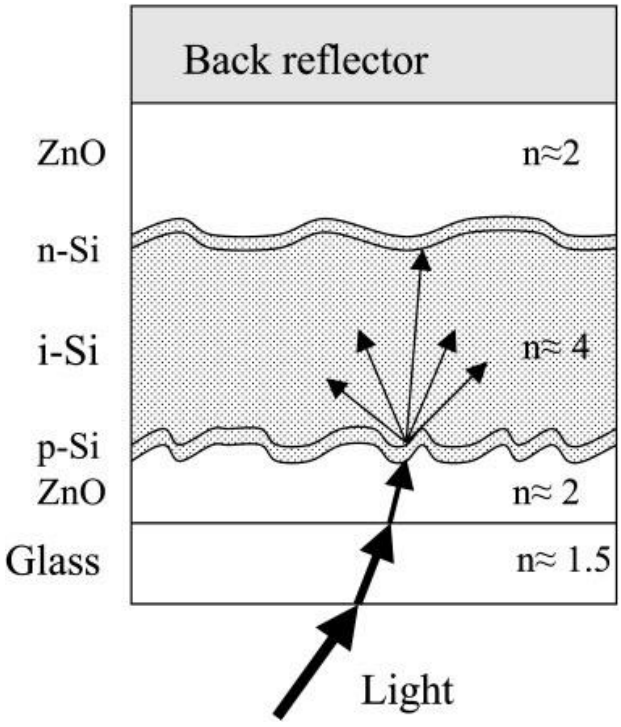

Figure 2-5, drawing of a silicon thin-film p–i–n solar cell (a-Si:H or µc-Si:H) with rough. Different light scattering and reflection events are demonstrated with small arrows indication diffused transmittance [14]. N is the refractive index value of each layer. Permission to reproduce this figure was granted by John Wiley & Sons.

The front TCO textures which occur as a byproduct of the deposition process, turned out to be a good scattering mechanism. Two famous examples for the superstrate cell type are the florine doped SnO2 and Boron doped ZnO (see Figure 2-6). Similar structures can be obtained from etching by one or more acids consecutively if sputtering deposition technique is used.

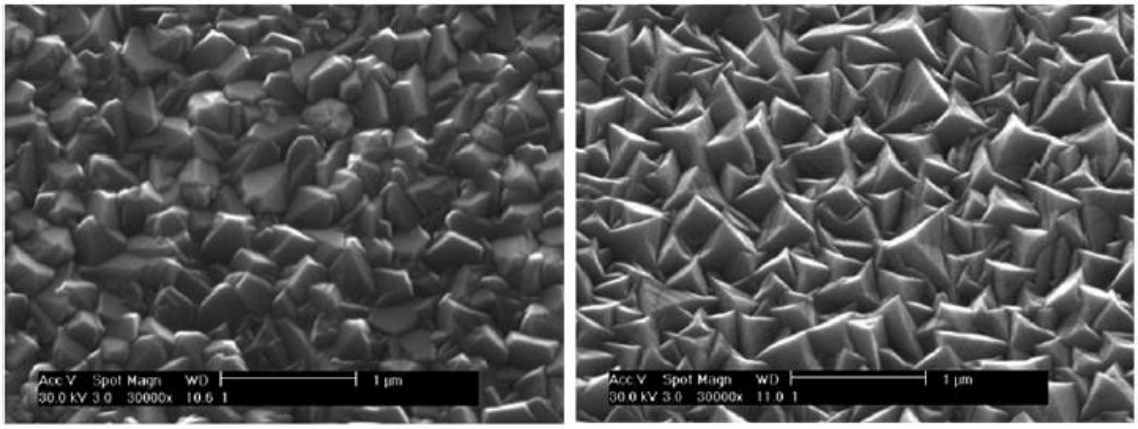

Figure 2-6, textures of florine doped SnO2 (left) and Boron doped ZnO (right)[28]. Permission to reproduce this figure was granted by Royal Society of Chemistry.

As explained in the previous section, a tradeoff between conductivity and transparency is needed in the TCOs, two different methods have been established by the famous EPFL (École Polytechnique Fédérale De Lausanne in Switzerland) PV research group[29-31] :

1. Bilayers of doped ZnO: The bilayers comprise a layer of around 200 nm thickness highly doped part, with smallest grains and hence more hindered conductivity because of high grain boundary density. The rest of the film, an order of magnitude larger (around 2um thick) have larger grains and hence better conductivity, is afterwards grown with no or low doping level. The resulting film has high transparency and strong light scattering in addition to good electric properties of mobility and sheet resistance.

2. H_2 Plasma post-deposition treatment: Hydrogen plasma treatment prompts enhanced electrical effects which are passivation of electron trap defects at grain boundaries, and an additional doping in the bulk of the grain. These electrical enhancements come without changing the optical transparency. H_2 plasma is also applied as post-deposition treatment on

thin-film silicon solar cells to enhance the electrical performance of the device by annealing the Si material, while increasing the conductivity of the ZnO back electrode.

The nip TFSSC, where cell is deposition sequence starts from bottom layers not facing the sun, the back reflector either is a metal which naturally has surface textures or the back reflector can be shaped to have different periodic shapes.

Scattering by metallic nanoparticles was proposed, and they proved to induce enhancements in some regions of the absorbed wavelength spectra due to plasmonics (highly localized oscillations of electrons). However the enhancement drops to less than one for the rest of the range making the overall effect not prominent.

One notable innovative design for better light management and scattering in addition to better electrical performance is the use of multiscale electrode features[32] (see Figure 2-7). A multiscale texture delivers light trapping and scattering over a broad wavelength range while at the same time insuring optimum morphology for the growth of high-quality silicon nanocrystalline layers. The design is tunable and the multiscale substrate is formed in two steps: first, a smooth and large-scale texture, fabricated in lacquer by nanoimprint lithography, provides scattering of high wavelengths of light for the bottom cell however conserving morphology suitable for high-quality silicon nanocrystals growth. Second, a succeeding 1 µm-thick, highly transparent LPCVD ZnO layer provides small and sharp features, ensuring coupling of lower wavelength into the top cell, once more with minimal impact on silicon growth.

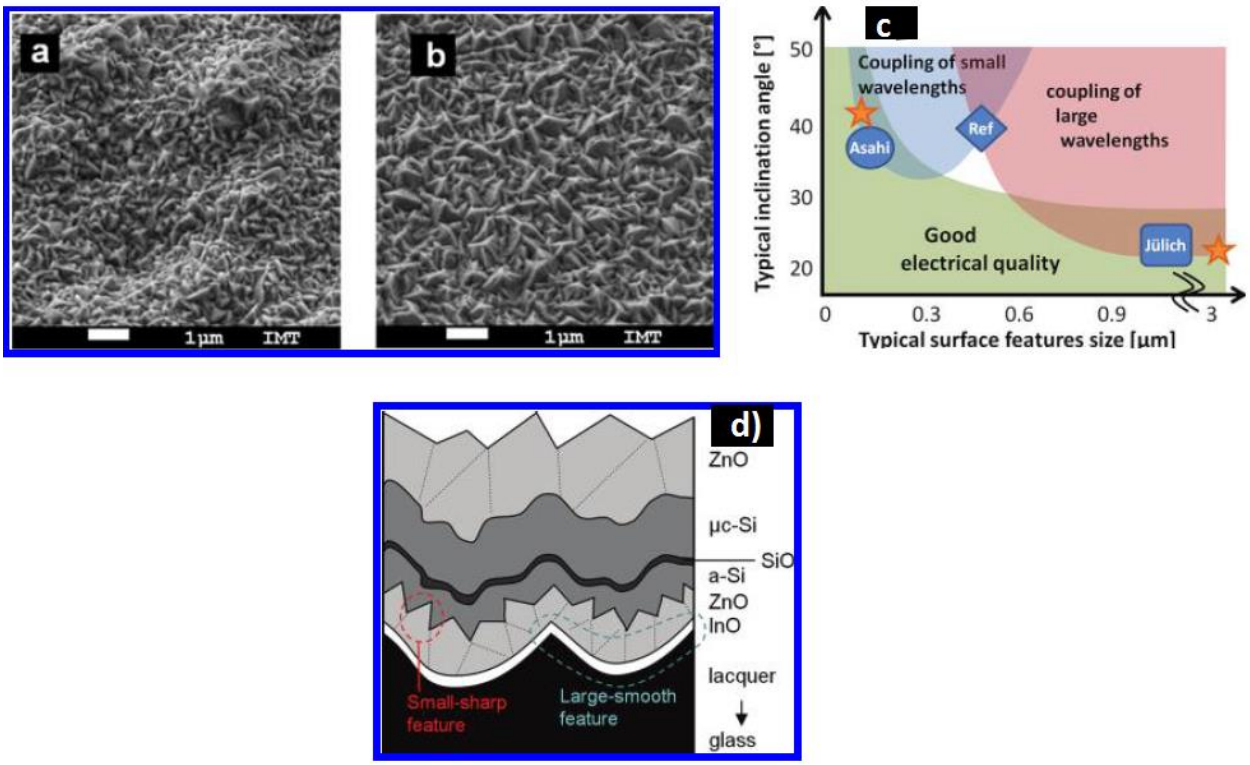

Figure 2-7, SEM images of the surfaces of the multiscale textured electrode (a) and the reference ZnO electrode (b). c) illustrate effect of two key morphological properties: size of surface size features inclination angle which is a measure of roughness. Three state-of-the-art TCO substrates are shown: tin oxide (Asahi), sputter-etched ZnO (Jülich), and LPCVD ZnO (ref). The stars outline to the two values used in the multiscale textured substrate.d) drawing with a cross section of a Micromorph cell deposited on a multiscale textured substrate demonstrating the small-sharp and large-smooth features[32]. Permission to reproduce these figure was granted by Royal Society of Chemistry.

2.3 Efficient use of sun irradiance

Any Solar cell suffers from two inherent types of losses related to the conversion of solar radiation to electricity: thermalization and waste of solar spectrum with wavelength larger than the bandgap of its active layer. The first, thermalization, is due to the difference in energy between the absorbed photon and the bandgap which is released as heat. The second, waste of solar spectrum with wavelength larger than the bandgap of its active layer, is due to the non-absorption of low energy photons (with energy less than the bandgap of the active layer).

One of the oldest solutions to these two problems is the use of different types of cell stacked on top of each other, with the upper cell absorbing higher energy photons. In the TFSSC, the micromorph tandem structure is an example.

Intermediate reflector layers (IRL) between sub-cells emerged to control the short circuits of each sub-cell. As the cells are connected serially, the resultant short circuit is determined by the lowest generated one and that's why current matching must be engineered. The IRL is composed usually of ZnO or SiO_x.

2.4 More on plasmonic enhanced solar cells, silicon nanowires and IRL

The three main design themes of the thesis depend mainly on plasmonic materials, silicon nanowires (SiNWs) and IRL respectively. The following two subsections will address these two techniques in a more detailed overview.

2.4.1 Plasmonic enhanced solar cells

Plasmonics is a key part of the relatively new Nanophotonics field. Plasmonics is based on the interaction between electromagnetic field and free electrons in a metal interface or in metallic nanostructures. Plasmonics enable confinement of electromagnetic fields into dimensions smaller than the wavelength of the exciting field and it has a lot of application in sensors, energy in addition to application that utilize sub-diffraction limit confinements such as waveguides, lithography and spectroscopy[33-37].

The two fundamental modes of plasmons are localized surface plasmons and surface plasmon polaritons (SPPs). The first are non-propagating excitations of the free electrons in metallic nanostructures coupled to the electromagnetic field. These modes arise in its simplest form from the scattering of sub-wavelength nanoparticles in an oscillating electromagnetic field. The second is SPPs, which are electromagnetic excitations propagating along a metal/dielectric interface, and evanescently confined perpendicularly to it (see Figure 2-8).

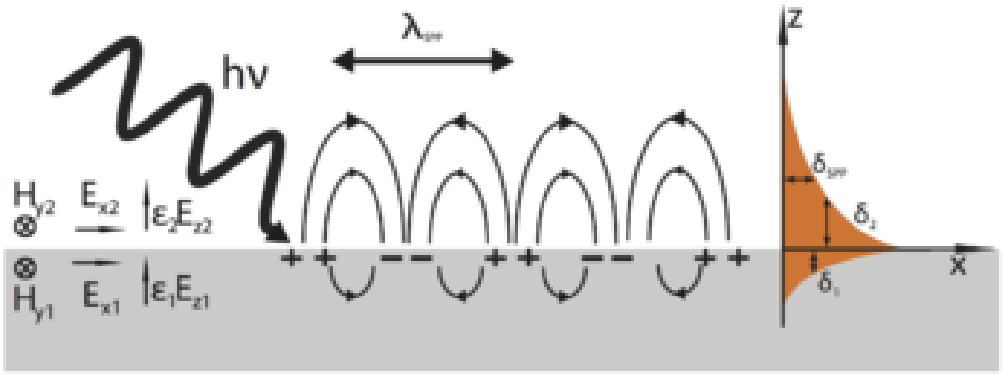

Figure 2-8, surface charge density and field intensity of a propagating SPPs. Figure from https://en.wikipedia.org/wiki/Surface_plasmon#/media/File:Sketch_of_surface_plasmon.png

SPPs conditions can be derived from Maxwell equations, we can deduce that the field that cause the coupling must be a transverse-magnetic (TM) wave (magnetic field vector parallel to the interface plane) and they can exist only at interfaces between materials having opposite signs their dielectric constants real parts, i.e. they can exist at metal/dielectric interfaces.[34]

SPP field Intensity is at its highest value in the interface and decreases exponentially in the two interfaces with a much higher rate in the metal part.

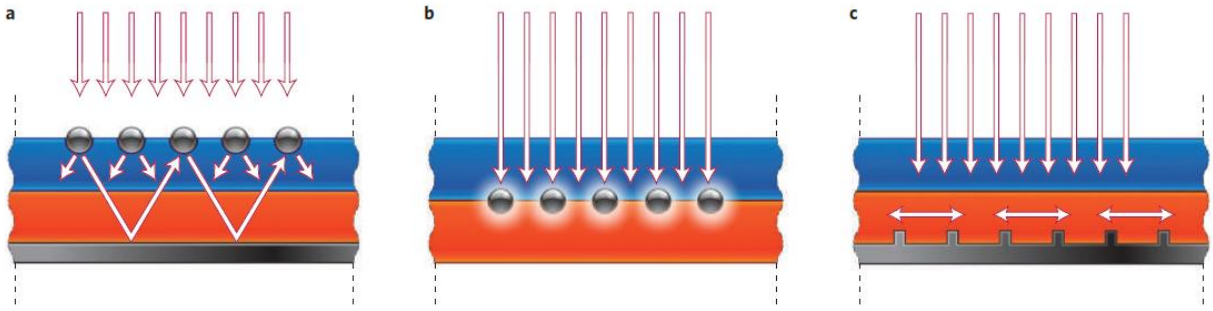

Figure 2-9, shows the three proposed ways plasmonics can enhance absorption in solar cells: scattering by embedding plasmonic nanoparticles in nonactive top layer, focusing light:by embedding nanoparticles in the active layer and SPPs light trapping by grooved metal back structure [39]. Permission to reproduce this figure was granted by Nature Publishing Group.

There is a potential for plasmonic enhanced solar cells to enable the use of ultrathin active layers and the topic has interested a lot of researchers. Plasmonic materials can enhance light absorption by[38,39] (see Figure 2-9):

a- Light scattering by plasmonic nanostructures: metal nanostructures with dimensions smaller than light wavelengths scatter and couple sunlight into the thin absorbing layer.

b- Light concentration by plasmonic nanostructures. Metallic nanostructures as will be illustrated can couple light to the active layer after increasing its effective absorption cross section.

c- Light trapping by SPPs. While the first two effects are usually performed by front (facing light) nanostructures, this effect is induced by grooved metallic layer on the back of the thin active layer couple the sunlight into SPP electromagnetic modes supported at the metal/semiconductor interface, in addition to guided photonic modes in the active layers.

It is worth noting that a common disadvantage of plasmonic applications is losses in the metal that might surpass the absorption benefits in the active layer[40].

2.4.2 Intermediate reflector layer (IRL) in TFSSC

Intermediate reflector layer (IRL) works as a spectrally selective layer between top amorphous cell and bottom nanocrystalline cell in micromorph silicon thin-film solar cell (see Figure 2-10). The IRL is usually thin, from tens of nanometers to around one hundred, and fabricated from transparent and conductive materials with a refractive index lower than that of the active hydrogenated amorphous silicon in the top cell.

A range of materials has been studied as IRs including even nonconductive (Lacquer) materials where electrical contact between is ensured by a limited covering [41] and the recently proposed hydrogenated mixed phase microcrystalline silicon oxide (μc–SiO_x:H). μc–SiO_x:H has the benefit of being deposited in the same deposition system of other silicon layers and its refractive index can be controlled from 1.9 to 3.7, in addition to maintaining good electrical conductivity[42].

IRL can be a simple single layer providing modest spectral selectivity. Other more complex realizations is a photonic crystal which provides a tunable optical band–gap to the required

wavelength range[42,43] . Recently, the tunable refractive index of µc–SiO_x:H has inspired researchers to propose alternating layers of µc–SiO_x:H having different refractive indexes to produce an easy to fabricate photonic crystal IRL[42].

Zinc oxide Intermediate Reflectors layer (ZIR) having different roughness values made by CVD or sputtering are also used[44]. In addition to relatively single layer ZnO, bragg reflectors and inverted opal structures were also studied experimentally and had promising results[43].

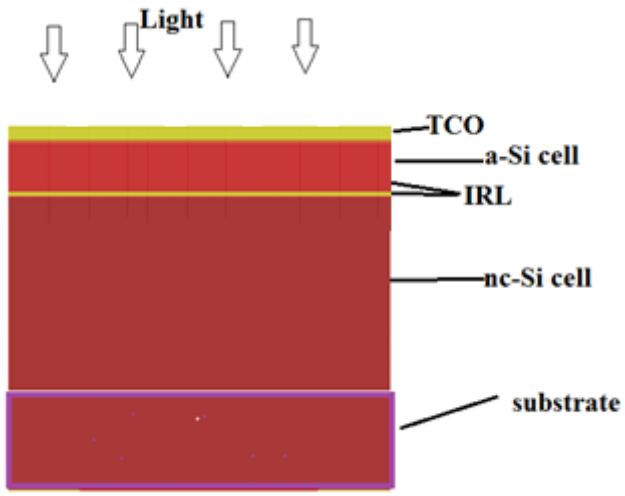

Figure 2-10, shows intermediate reflector (IRL) layer.

2.4.3 Silicon Nanowires and Nanocones texturing for photovoltaic applications

Relatively recent, a number of periodic and aperiodic nanostructures were studied both theoretically and experimentally showed very promising results, even though many suffer from enlarged recombination of photo-generated carriers.

Different facial nanostructures specially nanowires and nanocones (SiNWs and SiNCs) were fabricated by different techniques and had different levels of both periodicity and dimensions control. Fabrication methods includes etching with it different subtypes (metal assisted, RIE, alkaline and acidic) in addition to vapor–liquid–solid (VLS) growth and laser based fabrication.

SiNWs and SiNCs arrays have many advantages including its strong optical absorption in the solar wavelength spectrum, it is reported that less than 1% equivalent of Si materials in

SiNW arrays can realize the same absorption of traditional planar wafer-based PV devices. Second, if radial p-n junctions were utilized in the NWs, they offer a short collection length for charge carriers, accordingly tolerating the use of lower-quality Si materials. Third, many fabrication methods can greatly reduce production cost of Si based solar cell while still having excellent electrical characteristics [45,46].

3 SIMULATION TECHNIQUES

Opto-electrical numerical simulation of semiconductor devices in general is a well-known method for improving existing devices and designing new ones. The opto-electrical analysis results provided helps in earning insight into the devices physical operation, and can shed the light on parameters that needs improvement and allow designer to analyze the effect of several parameters simultaneously or one by one.

In the case of TFSSC, the workflow for a complete opto-electrical simulation is basically the same in all different academic and commercial device-simulation packages. First, optical simulation is performed to calculate spatial carrier density generated from the solar spectrum across the cell. Second, the calculated generation rates are fed into the electrical device simulation part that calculate short circuit current, open circuit voltage, J-V diagram and other electrical parameters.

As detailed below, in this work, we used a software package for optical simulations and another package from a completely separate vendor for the electrical simulations.

3.1 Optical simulations technique

Finite Difference Time Domain (FDTD) method for solving 3D Maxwell Equations is one of the famous methods used to optically simulate solar cells. Analysis of the whole wavelengths range can be done by one simulation carried in the time domain after calculating the frequency components of the EM waves is one of its strength. However one of the difficulties in using this method is fitting the optical indices to the models used by the program.

FDTD uses discretization in time and space to solve the 3D Maxwell equations. FDTD makes use of the fact that in the famous Maxwell equations, each of the E and H fields components depends on their previous values(from the time derivative part in the equation) in addition to the curl space function of the other field (E on curl H , likewise H on curl E). In the widely used Yee realization[47], the complete simulation area are divided into a grid where in each cell (Called Yee cell) the Electric and Magnetic field components are organized such

that each vector component is positioned between a pair of the other field vector components (see Figure 3-1). Yee realization also uses a trick to simplify calculations; the E and H fields time-stepping calculations are done such that each field is calculated midway during each time-step between successive H-field updates.

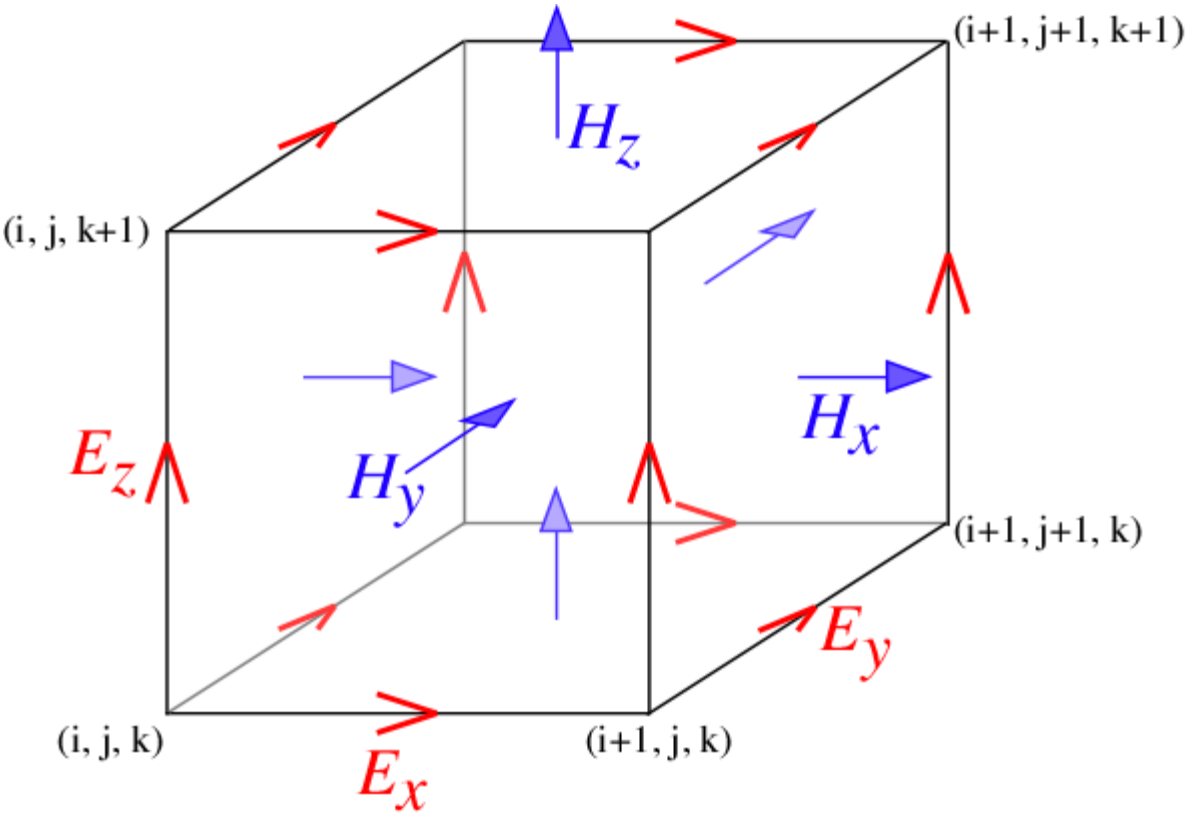

Figure 3-1, graph illustrating Yee cell with positions of E and H fields components illustrated. Yee proposed E components on the midway between edges while H components in the middle of faces. Graph from http://ab-initio.mit.edu/wiki/index.php/Image:Yee-cube.png (GFDL licensed)

In this thesis, Lumerical[48], a commercial FDTD software package, was used to calculate the 3D carrier generation profiles and photo-generated current densities in addition to the Electric and magnetic fields profiles.

3.1.1 FDTD Practical issues

In this subsection, several practical issues related to the simulations performed are discussed.

3.1.1.1 Unpolarized light and how it is accounted for:

FDTD simulations have well defined polarized sources and to calculate the response due to the unpolarized sun irradiance, we need to incoherently average two perpendicular plane-wave source polarizations. However, in symmetric structures only one simulation is sufficient.

3.1.1.2 Material fitting:

One of the main advantages of FDTD as explained before is the ability to perform wide range wavelength response analysis with one simulation; however, this is true if the materials used were accurately representing the dispersive values of each material optical indices along all the wavelength range of interest.

As we are concerned with linear isotropic materials; Drude, Debye, Lorentz or a combination of them are traditionally used to describe the dispersive nature of the optical materials. Although that gives a good insight into the behavior of the materials, these models doesn't easily fit experimental values for the wavelength range of interest.

While using a combination of models or the summation of multiple resonances in the same model may fit the dispersive material in an accurate way, it affects the simulations time and sometimes can lead to simulation convergence problems. The commercial software package used in this thesis has its own proprietary material fitting technique called the multi-coefficient models (MCMs). MCMs uses a set of basis functions to better fit material dispersion values without requiring the user to do it on his own while still leaving some control(see Figure 3-2).

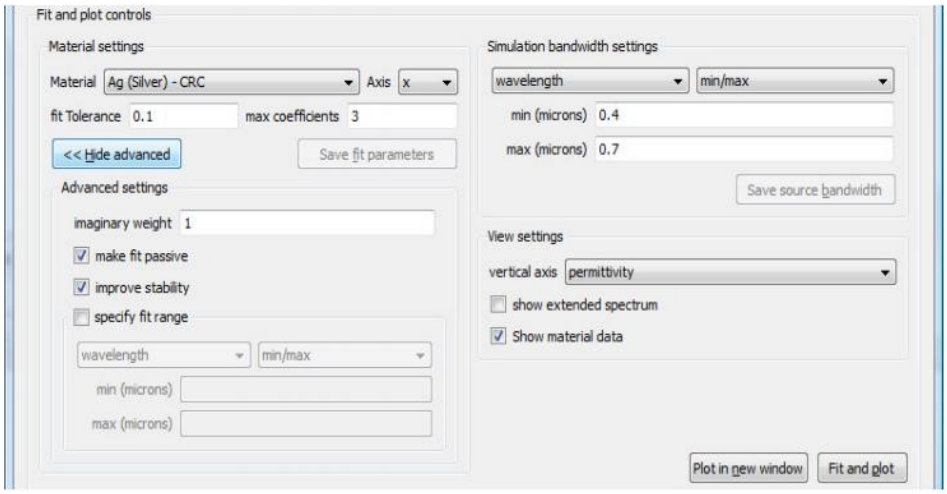

Figure 3-2, material fitting window in the used FDTD package where users can specify some upper level control on the fitting process in addition to checking the fitting results.

3.1.1.3 Boundary conditions: PML, periodic, symmetric and antisymmetric

The structure simulated must have defined dimensions which are divided into discrete cells as explained before. The following boundary conditions were used:

- Perfectly matched layer (PML) : This is used to define open or non-reflecting boundaries, for example, air.
- Periodic: Used to define boundary conditions for periodic structures and EM fields.
- Symmetric and/or Antisymmetric: used when structures exhibits one or more planes of electrical/magnetic fields symmetry.

3.1.2 Using FDTD to calculate Power absorbed and Generation rate

To calculate power absorbed as a function of wavelength, we utilize 3D electrical field and refractive index monitors and using the below equation

$$P_{abs}(\lambda) = \int \frac{1}{2}\, \omega . \varepsilon_0 . \varepsilon_{imag}(\lambda) . |E(\lambda)^2|\, dV \qquad (1)$$

Where ω, ε_0, ε_{imag} and E are the angular frequency, permittivity of vacuum, imaginary part of the active layer dielectric constant and electric field, respectively. By normalizing the result over the incident power at each wavelength, the percentage of power absorbed is calculated.

After calculating the percentage of power absorbed as a function of wavelength, which is equal to External quantum efficiency (EQE), the photo-generated carrier current density can be calculated using the following equation:

$$J_{ph} = e \int EQE(\lambda).\phi_{AM\ 1.5}(\lambda) d\lambda = \frac{e}{h.c} \int \lambda.EQE(\lambda).I_{AM\ 1.5}(\lambda) d\lambda \quad (2)$$

Where e, h, and c are the electron charge, Planck's constant and speed of light respectively, while ϕ and I are the AM1.5 photon flux and solar irradiance respectively.

As for photo-generated carrier 3D profile which is used as an input to the electrical device simulator, the spatial power absorption at each wavelength is divided by the energy of each photon and integrated over the wavelength range using the following equation:

$$G(x,y,z) = \int \frac{1}{2} \frac{\varepsilon_0}{\bar{h}} \varepsilon_{imag}(\lambda).|E(\lambda,x,y,z)^2| \, d\lambda \quad (3)$$

The method described above is relatively time consuming and resource intensive, another simpler method was utilized. In addition to being simple, it delivers accurate results in simple flat structures or if active layers are surrounded by low loss materials. The method proved to be valuable in initial design optimization and to get a sense of the effect of the dimension of different layers, IRL or front TCO for example, on the generated current densities. Using two 2D power monitors placed above and below the active Si layer for each subcell, sometimes encompassing non-active layers also when the structure is not flat. The percentage of power absorbed by the volume surrounded by the two monitors are calculated by subtracting the power transmitted from the lower monitor from the other upper monitor facing the Optical source. After normalization, we can proceed with calculating photo-generated current density and other parameters as outlined in the first method.

For micromorph cell, simulation of the relatively large wavelength range from 350-1100nm is needed. Although one of the main advantages of FDTD simulation is calculating broadband results from a single simulation, this advantage has a condition that material optical indices fitting are correct all over the wavelength range. Due to the large difference in the

imaginary part of the dielectric optical indices of the active layers across the wavelengths range, all efforts to fit them in the whole range were not successful and the simulations were divided into three regions chosen by trial and error for better fitting (350:600nm; 600nm:900nm and from 900nm to 1100nm).

3.2 Electrical simulation techniques

Unlike crystalline based solar cells, the electrical simulation of TFSSC is much more complex due to the atomic structure of the constituents. There is no clear conduction band or valence band and the charge carriers have continuous density of states. Some academic research groups have designed their own programs for modeling TFSSC from scratch[49], and usually these solve only 1D structures which sometimes can be tweaked to simulate 2D or 3D structures. Other commercial tools have the flexibility to simulate 3D structures[49].

In the thesis, Sentaurus device simulator was used[50]. Sentaurus is a modular program that has very wide simulation capabilities in contrary to other ones developed by Academic research groups which are usually specialized. As a general purpose device simulator, Sentaurus simulations need to be tested and compared to results from literature. Sentaurus also is very computer resources consuming specially for 3D simulations. Finally, the time required to master the program is very slow compared to other specialized TFSSC programs.

Optically-generated charge carriers were fed in the program using typical doping values and other TFSCC electrical modelling parameters taken from several references. For simplicity and due to conversion problems and time intensive simulations, we simulated each a-Si and nc-Si subcell separately.

3.2.1 Electrical properties of a-Si and nc-Si

Electrical modeling of thin-film silicon devices in general is different from crystalline based ones due to their different atomic and electronic structures. Silicon atoms in amorphous layers suffer from short ordered regions with different bond angles and lengths in contrary to the crystalline form[51,52]. Si atoms also suffer from dangling (missing) bonds which are usually overcome by using hydrogen in the deposition process[51,52] as shown in Figure 3-3.

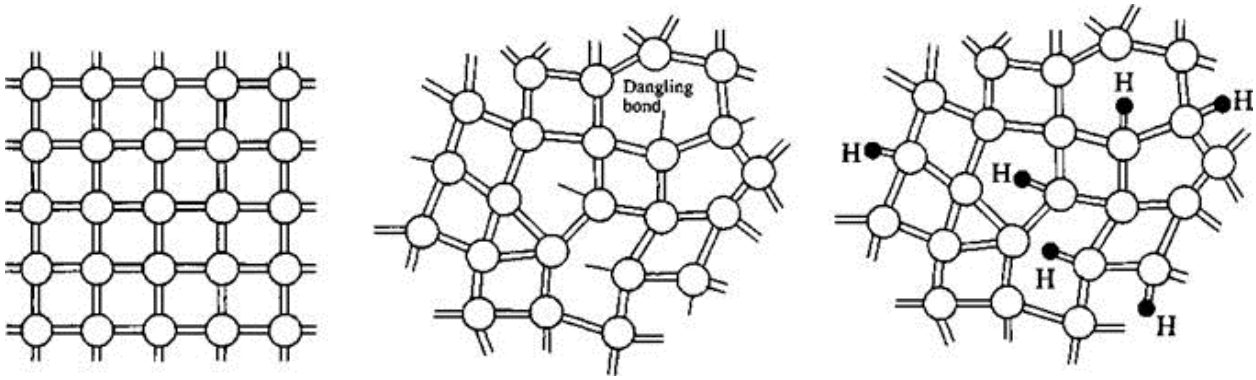

Figure 3-3, schematic structure of Si atoms in the crystalline, amorphous and hydrogenated amorphous forms. The hydrogen atoms as shown in the rightmost diagram help passivate a high percentage of the dangling bonds.[53]

The lattice defects in the amorphous silicon layers leads to "tails" in the conduction band and valence band edges in addition to a large number of middle gap states in contrary to the crystalline clear cut bands and the almost non-existing middle states. In our case, we define mobility gap which distinguishes the extended states above the conduction band edge and below the valence band one from the localized states in between (see Figure 3-4). The mobility of carriers in the extended states is much greater than the localized ones[51,52].

The carriers transport in the amorphous layers are influenced by three main processes: traditional extended states carrier movements, multiple trapping and multiple hopping. The multiple trapping occurs when a carrier in the extended state is captured by a localized state, which will later reemitted to the extended state after being immobilized during the stay in the localized state. The hopping, which is more profound in low temperatures and not taken into account in solar cells case, occurs when carriers hop between different localized states[51,52].

The above illustrated electrical properties leads us to the fact that we must take into account the recombination and localized trapped charges in the electrical device simulation. Although the Density of state (DOS) is very complicated, a DOS model is usually used to reflect experimental values. The DOS is divided into parabolic conduction and valence bands, exponentially decaying conduction and valence band tails, and two Gaussian regions in the middle of the mobility gap which models the effect of dangling bonds[51,52] (see Figure 3-4).

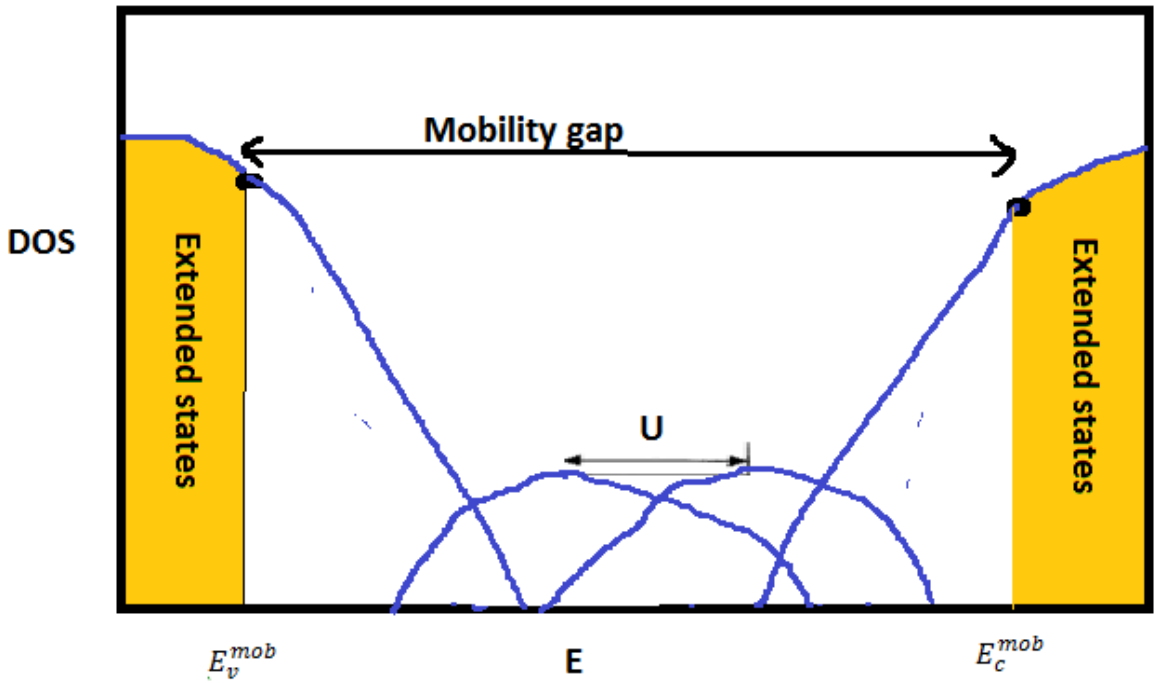

Figure 3-4, a schematic of the standard model of the DOS of a aSi:H layer on a logarithmic scale. The tail states of conduction and valence bands can be seen in addition to the two Gaussian distributions representing the dangling bonds amphoteric states [54].

In the standard DOS model, Mobility gap is defined by the energy of the mobility edge of the conduction band E_c^{mob} and the mobility edge of the valance band E_v^{mob}. The states in the mobility gaps are localized and are represented in the three following regions: the conduction band tail modelled by an ordinary acceptor like states, the valence band tail modelled by ordinary donor like states and the last region models the amphoteric nature of defect states(positive, negative and neutral) using two energy levels with Gaussian distributions (donor $D^{+/0}$ and acceptor donor $D^{-/0}$)to model the amphoteric nature. The separation of the two Gaussian distribution is called the correlation energy U[51,52].

When electrically simulating TFSSC, the same basic semiconductor equations are used in the device simulation programs, the main distinctions from crystalline materials simulations are the carrier recombination calculations and the trapped charge carriers which plays a significant role in a-Si. For example, in the Poisson equation, the space charge density ρ is equal to ($p-n+p_{local}-n_{local}+N_{don}-N_{acc}$) and that takes into account the localized charge carriers ($p_{local}-n_{local}$) and the ionized donors and acceptors atoms[51,52].

The recombination of carriers in the mobility gap region is also much more complicated than the crystalline materials which often have a single energy level recombination center in the energy gap. In the amorphous case, recombination is calculated by integrating the contribution of the continuous DOS in the whole mobility gap area.

3.2.2 Overview of Synopsys TCAD

Technology Computer-Aided Design (TCAD) refers to the use of computer simulations to design semiconductor processing technologies and devices. Synopsys TCAD suite is a well-known broad suite of products that includes sophisticated and leading process and device simulation tools.

The following TCAD tools were used in the simulations:

1. Structure Editor: this tool is a sophisticated structure editor for 2D and 3D device structures. Which has a graphical user interface (GUI) and is used to create complex structures using 2D or 3D basic structures, such as rectangles, polygons, cylinders, and spheres. More Complex shapes are generated by intersecting basic elements.
2. Sentaurus Device: is a modular device simulator that can simulate a wide range of electrical, thermal, and optical characteristics in a wide range of materials.
3. Sentaurus Data Explorer: is a tool for editing and converting data from/to simulations and across different data types. This tool was used to input the carrier generation rate from Lumerical to Sentaurus device.
4. Inspect: Inspect is a plotting and analysis tool and was used to calculate Voc, Jsc and draw JV graphs.
5. Sentaurus Visual: plotting tool for visualizing data like doping, generation rates and other physical values.

3.3 Integrating Optical and electrical simulation

Due to the complexity of Optical and Electrical simulations, an efficient method was used in the IRL design part of the thesis to combine the highly sophisticated optical simulator

Lumerical with the outstanding electrical simulation capability of Sentaurus. This section addresses integrating Lumerical and Sentaurus to simulate 3D structures opto-electrically and was based on a previous Work by Michael Kelzenberg in his Thesis "Silicon Microwire Photovoltaics"[55]. The work addressed integration of 2D structures and it was used as a base to simulate our IRL 3D structures opto-electrically.

Sentaurus Device, the electrical simulator used, utilizes a finite-element mesh different from the one used by Lumerical. The integration of the two separate packages is achieved by data extraction using Sentaurus Data Explorer tool and data mapping to the mesh used by Sentaurus was done using a MATLAB script modified from the above mentioned work to perform 3D mapping as shown in Figure 3-5.

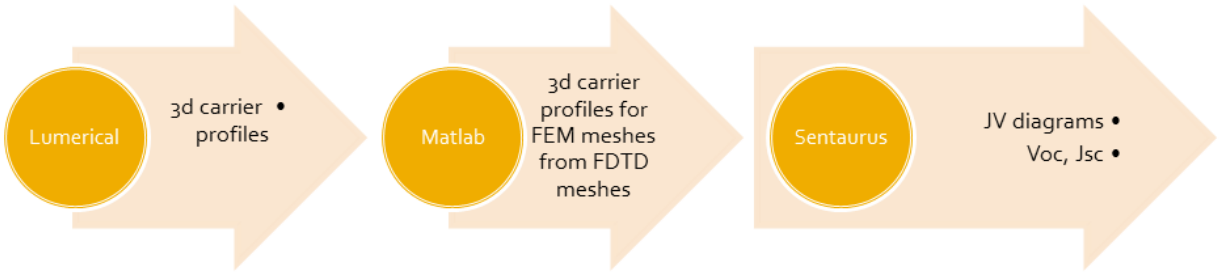

Figure 3-5, flow-chart of the opto-electronic simulation method. Lumerical, Matlab and Sentaurus device simulator package are used.

In the appendix, the complete Matlab script used is shown.

4 NOVEL DESIGNS FOR THIN-FILM SILICON SOLAR CELLS

4.1 Design 1: optical Study of TiN as a back reflector for a-Si solar cells

In this section, titanium nitride (TiN), which has proven plasmonic properties, is studied as an alternative plasmonic material for silicon (mainly amorphous) solar cells. TiN is much cheaper than silver or gold and is silicon manufacturing processes compatible and it would be very beneficial if it had opto-electrical performance comparable to that of silver, the metal famous for good reflectivity and plasmonic properties in the wavelengths range of silicon absorption.

This chapter is based on two papers, a conference and journal[56,57]. The focus is mainly on back plasmonic reflector for a-Si:H, although other structures are briefly studied.

4.1.1 TiN plasmonic properties

Recently, it has been shown that titanium nitride (TiN) has good plasmonic properties in the visible and near-infrared regions[58,59]. The excitation of surface plasmon polaritons on TiN thin-films was successfully demonstrated, and exhibited performance analogous to that of gold for plasmonic applications. TiN is nonstoichiometric, therefore, the optical properties depend on the substrate over which the TiN layer is grown, and also on the deposition temperature and conditions in addition to the substrate where the film is grown onto (see Figure 4-1 and Figure 4-2).

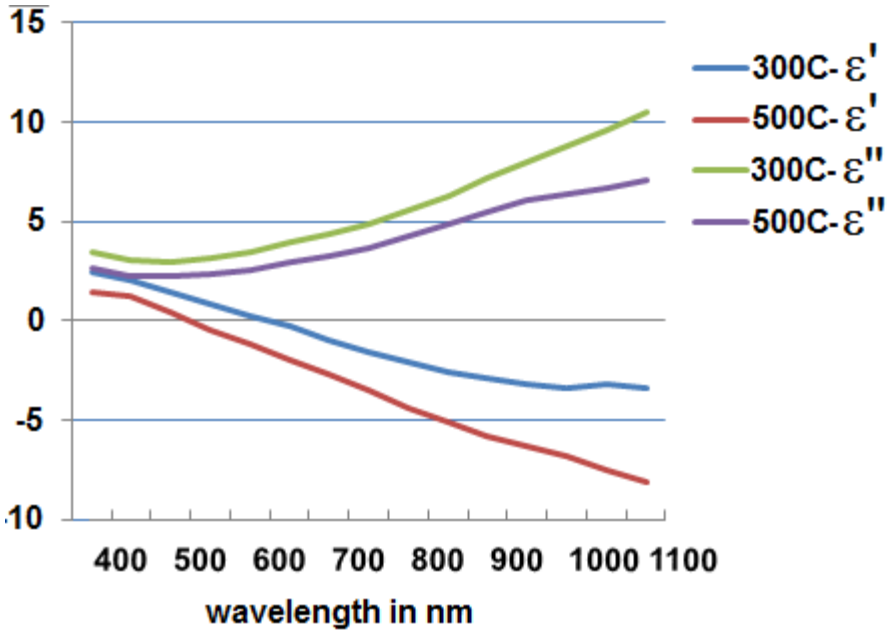

Figure 4-1, shows effect of deposition parameters and substrate on the Dielectric function of TiN films. Dielectric functions of titanium nitride films deposited at 300 ^{o}C and 500 ^{o}C based on data from [59]

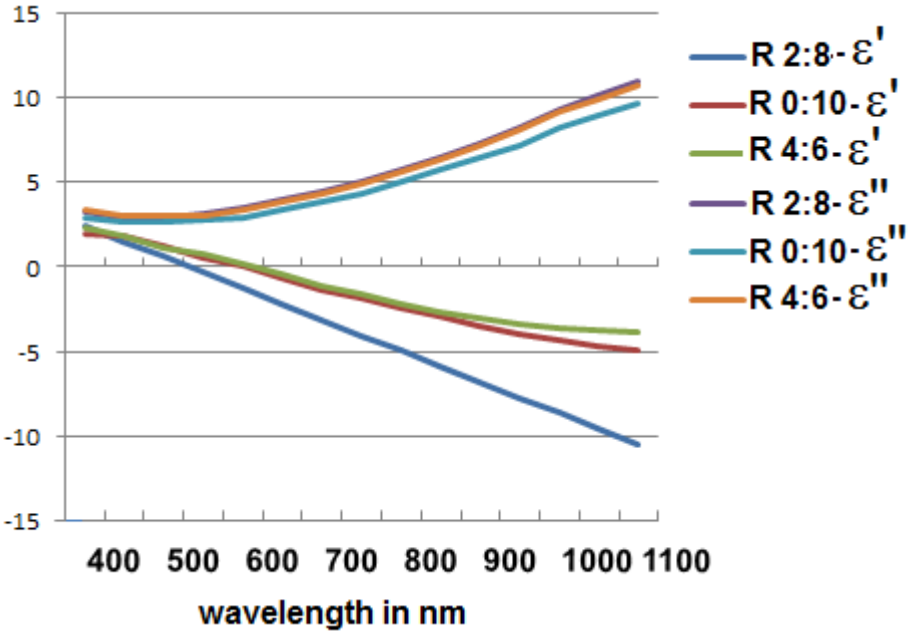

Figure 4-2, shows effect of Argon:N_2 flow ratio (R) on the Dielectric function of TiN films deposited on c-sapphire substrates at 300 ^{o}C based on data from [59].

4.1.2 TiN as an a-Si back plasmonic reflector

Silver nano-periodic structures on the back of a-Si solar cells, exhibited significant short circuit current increase in TFSSC, according to many theoretical and experimental studies. Due to the deposition of the cell on top of the silver nano-structures, subsequent deposited layers for example a-Si and front TCO have similar conformal nano-structures.

The comparative study approach is using one of the well-known studied silver nanostructures[60] and replace the silver with TiN to study the performance change. The structure comprises a silica substrate with protruding periodic half nano-spheres repeated periodically. The successive layers of silver, ZnO, a-Si and ITO are conformally deposited on top of the substrate as shown in Figure 4-3. The structure has a period of 250nm.

For computing the power absorbed and the J_{sc} current density generated in each layer, other details and techniques to those previously outlined in the simulation chapter were utilized. First, as the whole cell structure is symmetrical, only one simulation is utilized for each analysis using a broadband plane wave source located 200nm above the ITO layer. Second, due to periodicity, only one period of the structure is simulated and FDTD periodic boundary condition is utilized on all boundaries, except for the upper and lower ones, where perfectly matched layer (PML) boundary conditions are utilized, and that to imitate the semi-infinite air above and below the cell.

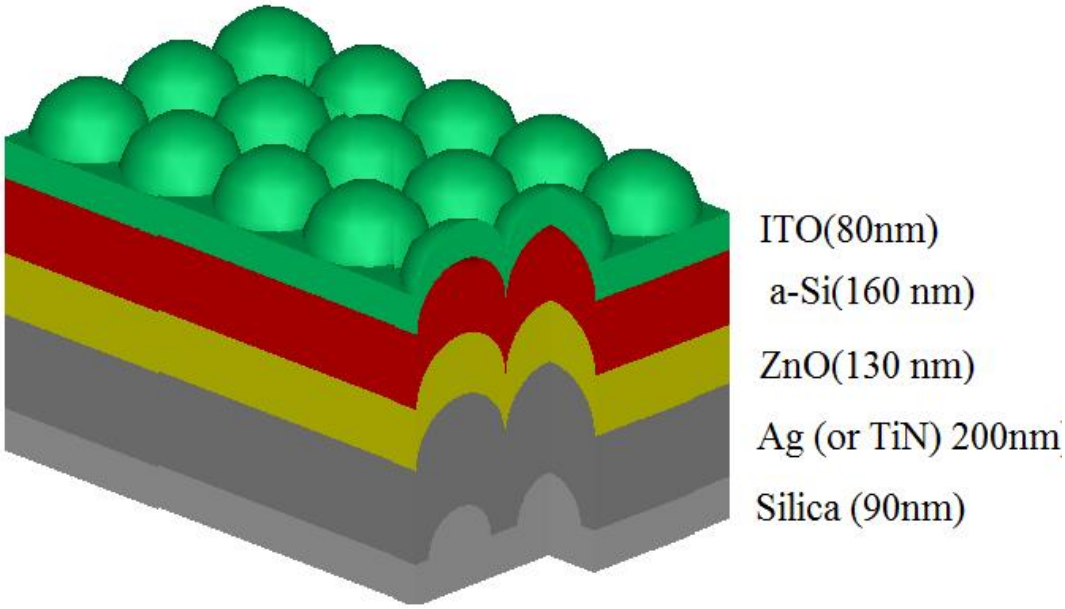

Figure 4-3, nanostructured TFSSC used for comparative study. Half nano-spheres have 250nm diameters for all materials, except for the silica substrate (175nm).

To gain insight on the optical performance of the two compared cells, power absorbed in each layer throughout the 400-800nm wavelength range was computed(see Figure 4-4). The spectral response in the wavelengths range from 400-600nm is almost identical while the rest of the range is not, hence the spectral response can be divided into two regions. The first one, from 400nm to 600nm spectral range is more or less equal due to high absorbance of the a-Si at this wavelengths range, so almost no light passes to the ZnO or any layer below. However, the second range, with wavelengths range from 600 to 800nm, has easily spot increased absorption of the TiN layer relative to its silver counterpart, and the latter had in turn an increase in the power escaping by reflection.

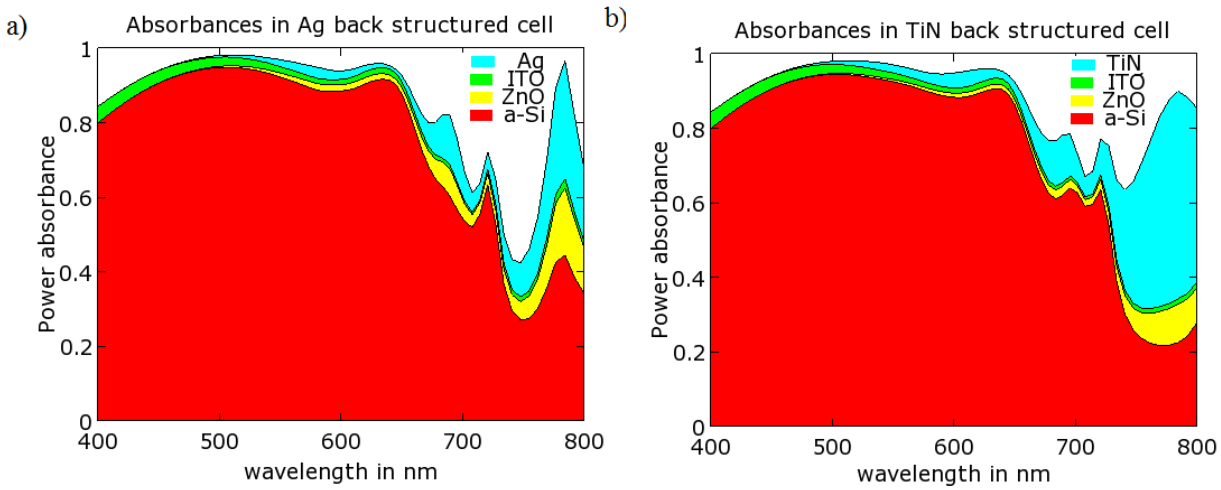

Figure 4-4, fraction of power absorbed in each layer of a-silver, b-TiN based cells (white part amounts to the power escaped from the structure by reflection).

Comparing real refractive index of TiN and silver can give an answer to the comparatively high absorption calculated in TiN layer in the 600nm to 800nm spectral range. TiN has high real refractive index which is around 0.9, while that of silver is less than 0.15(both have comparable imaginary refractive index). Using Fresnel reflection equation ($R=|(n-1)/(n+1)|^2$) for a normal incident wave in vacuum, as a reference for reflectivity, we can realize that TiN relatively high real refractive index makes it reflect less light, with more light transmitted into it and absorbed.

Three more simulations were done to study the number of passes that light make through each of the three structures (silver and TiN periodic ones in addition to the flat silver cell). Time analysis of cells with a broadband pulse source having spectral range only from 600-800nm was utilized. A power time monitor to measure reflected optical power was placed before the top PML boundary to study the number of passes the light makes in the three cells. The monitor was placed 200nm above the source which has a pulse width of almost 18fs (see Figure 4-5).

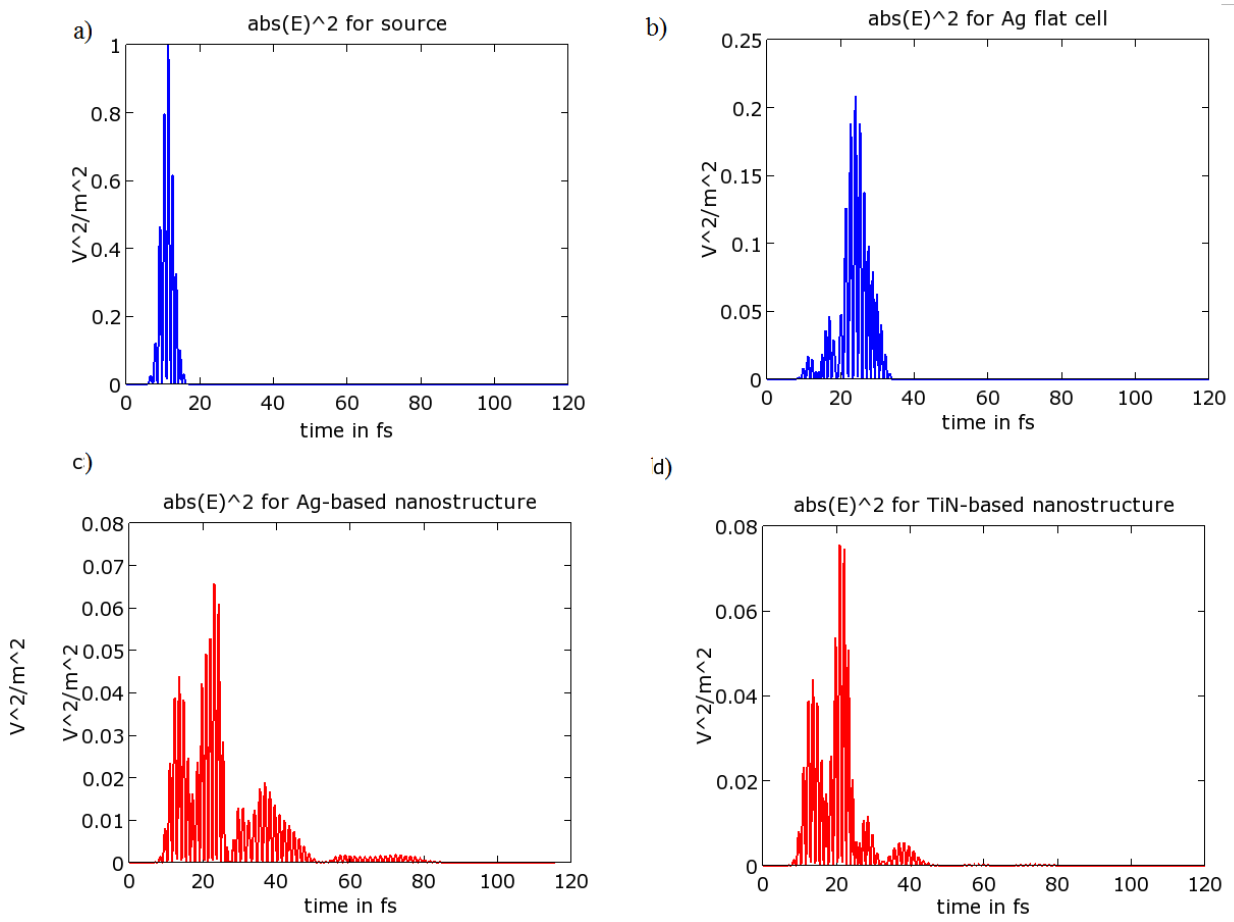

Figure 4-5, a- graph of the source pulse utilized in simulation, b-d square of the E-field magnitude at a point above the flat cell, silver periodic cell and TiN periodic cell respectively.

Studying the above graph of the square of the E field magnitudes for power monitors of the three cells, we can deduce several significant features of the three cells. First, the flat structure suffers from high reflection and hence optical power escaping the flat cell. Second, in the non-flat cells, we can notice much lower power reflected and the occurrence of several peaks, one at around 14fs and another one at around 22 fs and then smaller ones with relatively smaller magnitudes. The initial peak, at around 14fs is due to reflectance by the upper ITO surface, while the second, which has larger magnitude is attributed to the field that travelled one round-trip inside the cell then got transmitted from the ITO to air. Succeeding peaks are also attributed to escape of field from subsequent round-trips.

Using the above analysis, we can deduce that the strength of the periodic structure is attributed to low initial reflection and the scattering of light rather than enabling multi-pass through the structure.

Also to verify the distance between peaks, a simplification can be made, where we can assume that the effective medium of the cell is around 3 and hence the time it takes for light travelling a path back and forth after being reflected from the silver(TiN)surface can take the range from 10-15 fs, which agrees with the graphs .

For the design, dielectric constants used for ITO and Aluminum doped ZnO (ZnO:Al or ZnO for brevity) were 2.08+0.004i and 1.93+0.004i respectively[61], while TiN and a-Si:H dielectric constants was taken from Ref [62]and silver from Palik famous optical constants handbook[63]. It is worth noting that the a-Si:H optical constants used have higher absorption coefficients than that reported by other literature[64] and this can account for the relatively high J_{sc} currents computed. In the designs discussed after this section, experimental values of a-Si:H optical constants from Ref.[64] were used.

4.1.3 Comparing Optimized back structures of TiN and silver

In the journal paper, the effect of different sphere dimensions on the J_{sc} density was studied. Through an optimization procedure detailed below, it was found that the conformal spheres having a diameter of 216 nm and a period of 366 nm for the whole structure produced the best J_{sc} result for the silver-based structure ($17.96\ mA/cm^2$). On the other hand, the optimization of the same structure with TiN replacing the silver is obtained with a diameter of 216 nm and a period of 266 nm and produced a J_{sc} of $16.85\ mA/cm^2$.

We designed a fast and moderately accurate optimization process to find the above mentioned optimal cell design for both the silver-based and the TiN-based structures using a brute force search. Diameters from 100 to 250 nm and periods from 100 to 400 nm were simulated and J_{sc} maps are plotted (see Figure 4-6). The less computer-intensive method discussed before in section 3.1.2 was used for calculating the absorbance in the a-Si and hence

the short circuit. Using this method provides a fast and effective way to scan possible diameters and periods, although the results are less accurate than those obtained using the other method.

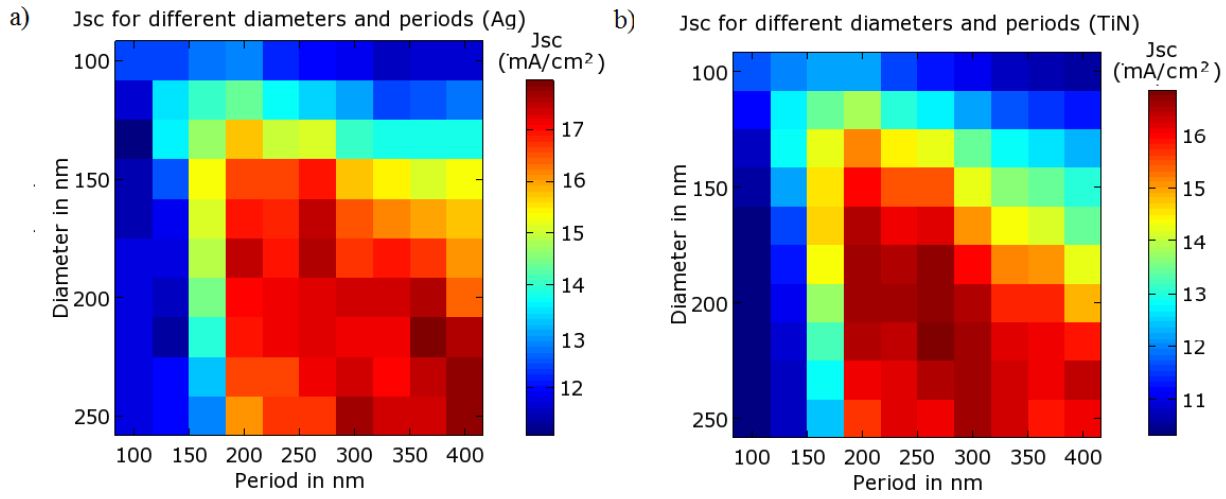

Figure 4-6, J_{sc} density maps for different dimaters and periods of the a) silver and b) TiN periodic back structures.

The other method, discussed also in section 3.1.2, was utilized to calculate the J_{sc} density for only the optimal structures. The optimal current for the silver-based solar cell was 16.32 and was $15.95\ mA/cm^2$ for the TiN-based one, which is very close to its silver counterpart.

Due to the complexity of the structure and the nonuniform nature of the AM1.5 sun irradiance, the effect of changing the diameter and period of the structure on the J_{sc} is highly nonlinear and does not have a well-defined trend. However, to gain more insight into the absorbance of each layer, we calculate, using the more accurate method, the absorbance of each layer in each of the two optimized TiN and silver cells. We can see that from the 350 to 500-nm spectral range, absorbance is almost the same in the two cells. In the rest of the simulated spectral range (500 to 750 nm), there is a difference in the absorbance of TiN and silver, although the absorbance in the a-Si layers is very close (see Figure 4-7).

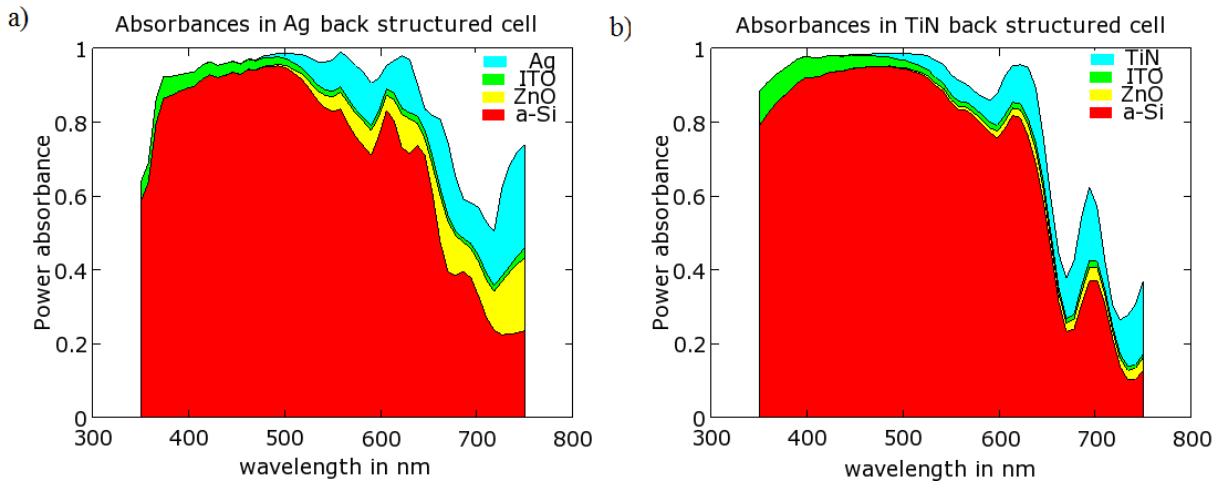

Figure 4-7, Percentage of power absorbed in each layer of a-silver, b-TiN based cells, with the white part representing the power escaped from the structure by reflection.

To gain more insight into the effect of plasmonic materials on the structures, the two optimized structures were simulated without any plasmonic material (no TiN or Ag). In the optimized Ag cell, a J_{sc} of 17.31 mA/cm^2 was calculated after completely removing the Ag bottom layer. For the case of the optimized TiN cell, a J_{sc} of 17.32 mA/cm^2 was calculated after completely removing the TiN bottom layer. These two results indicate that the conformal spheres' structure has good optical properties.

4.1.4 TiN based top plasmonic solar cell structures

A study in Ref. [65] revealed that gold nanoparticles placed on top of a silicon PN junction enhance absorption in longer wavelengths and deteriorate the performance at shorter wavelengths due to the large phase difference between scattered and original incident wave below the SPP resonance wavelength. Although reported on gold, this behavior applies to other plasmonic metals[66].

By incorporating the TiN spherical nanoparticles on top of crystalline silicon substrate and comparing to the EQE of a bare crystalline silicon substrate, we can graph the enhancement in absorption (g) as a function of wavelength which is the ratio of the EQE of the structure with

TiN top nanoparticles over the same bare structure, where EQEs are calculated using the less computer-intensive method, i.e.

$$g(\lambda) = \frac{EQE_{top\ TiN\ nanoparticles}(\lambda)}{EQE_{bare\ structure}(\lambda)} \quad (3)$$

Figure 4-8a shows this enhancement for a period of 400 nm and different diameters and as expected the graph clearly shows absorption enhancements at long wavelengths roughly exceeding 700nm.

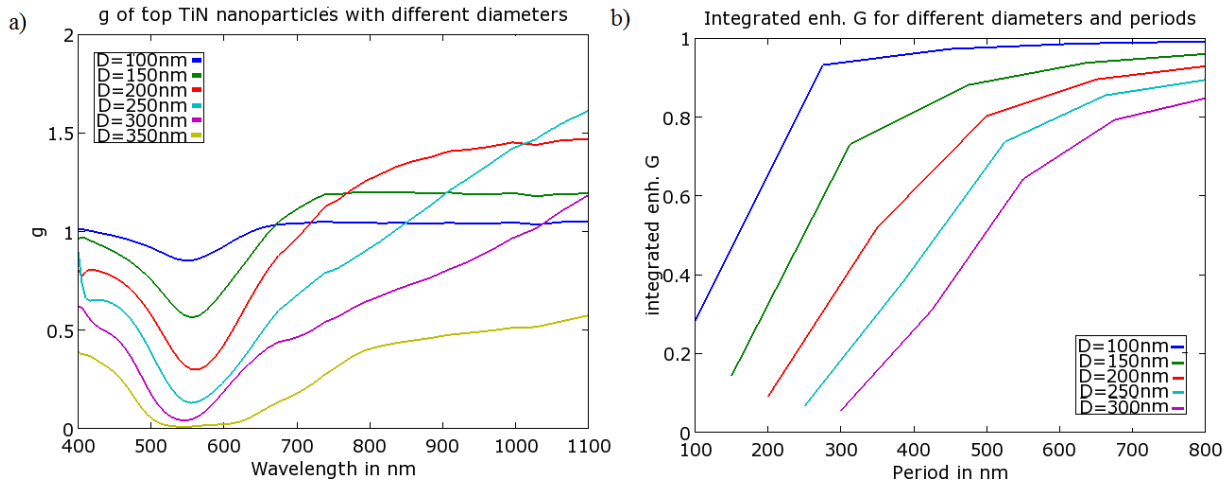

Figure 4-8, a-absorption enhancements for nanoparticles having different diameters and a period of 400nm. b-total enhancement G for different diameters and periods.

As the absorption enhancement is not constant along the whole solar spectrum which in turn has different irradiance at each wavelength we need to calculate the overall effect of introducing the TiN top nanoparticles. This overall effect of the nanoparticles can be calculated by dividing the J_{sc} of the structure with the nanoparticles over the J_{sc} of the bare solar cell, this ratio is the overall or integrated gain enhancement (G), i.e. $G=Jsc_{\text{solar cell with nanoparticles}}/\ Jsc_{\text{bare solar cell}}$. The overall gain enhancement (shown as integrated enhancement G in Figure 4-8b) in absorption compared to bare solar cell structure with details of simulation outlined in Ref. [67] was thoroughly calculated, Figure 4-8b shows results for different TiN nanoparticles diameters and periods, and no combination has a good enhancement effect in contrary to silver and gold. To

compare the results with Ref. [65], same structure was utilized; the silicon substrate simulated thickness is 500 nm with perfect matched layer boundary condition.

The results of this subsection of top plasmonic nanoparticles are in accordance with the previously reported phase mismatch between scattered and incident light at wavelengths shorter than that of the surface plasmon resonance (SPP), and that is why they are not recommended by many authors [40,65,68].

Similarly, the effect of top gratings made from silver and TiN placed on top of crystalline silicon is studied. The simulated structure has gratings of a height of 150 nm and extended all over the substrate surface with a period of 400 nm. Grating widths of 100 nm and 200 nm were both simulated. As the structure is not symmetric, two polarizations are simulated for each material, s polarized field (E field is perpindicular to the gratings) results are similar to the above nanoparticle discussed while p polarized field (E field is parallel to the gratings) had poor performance in all gratings, so the overall accumulative effect is even worse than the nanoparticles placed on top. Comparing TiN and silver performance when placed as top gratings, it can be deduced that there is no substantial difference in their effects (see Figure 4-9 for gratings of 100nm width as an example).

The near-IR enhancements which didn't provide a good overall effect are anticipated to have an even worse effect when implementing top gratings on a-Si cells, as almost no a-Si absorption takes place in the near-IR range.

Al last, it is worth noting that ZnO has better reported trapping effect[69] when used as nanobeams, this can be attributed to low losses and the absence of Fano effect due to phase mismatch, which are present in all plasmonic materials.

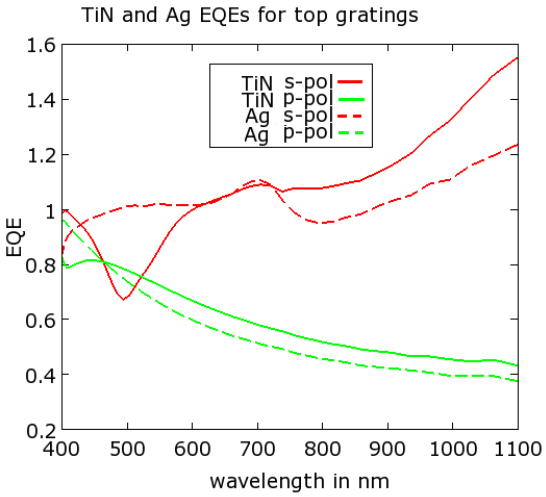

Figure 4-9**,** EQE for top gratings having widths of 100nm and a period of 400nm.

4.2 Design 2: Periodic optimized intermediate reflector layer

Intermediate reflector layer (IRL) functions as spectrally selective layer placed between top amorphous cell and bottom nanocrystalline cell in micromorph TFSSC. In the proposed design, matched short circuit current of both subcells reaches 13.6mA/cm^2 and even better results is anticipated if Lacquer material is used in combination with ZnO. In addition to optical analysis, basic 3D electrical simulation was performed and showed also good results. It is worth noting that the design procedure used can be easily applied to IRL composed of other materials and even to triple thin-films solar cells.

The proposed IRL is composed of ZnO:Al hemispheres on top of thin ZnO:Al placed between the two cells of the micromorph nip structure, better absorption can be achieved on the top cell while scattering can be enhanced in the bottom nc-Si cell. Figure 4-10 shows the structure as well as the three design parameters which are radii and period of the hemispheres in addition to the height of the flat part. It is worth mentioning that the bottom substrate was chosen to be a flat periodic optimized substrate (period = 1000nm) composed of an inverted n-type a-Si pyramid embedded in ZnO as proposed by [70] to achieve best results, although we anticipate that any optimized substrates will have close results.

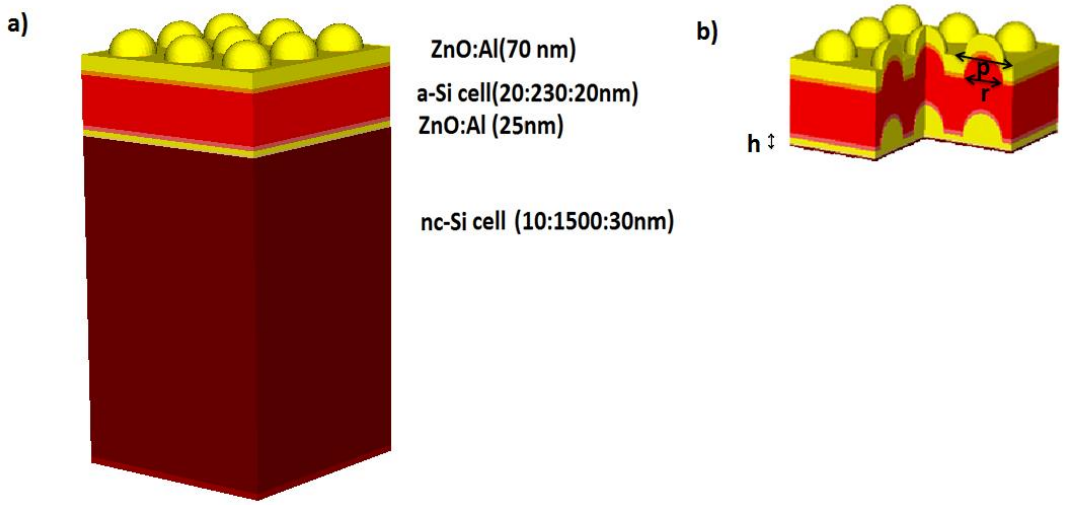

Figure 4-10, a)3D Diagram of the whole micromorph cell, b)cross section through the cell showing hemispherical top a-Si:H structures on an entirely flat bottom nc-Si sub cell. h,p and r are the three parameters of the proposed structure and represent height of the flat part, period and radius of the hemispheres respectively. The substrate is not shown and dimensions of each cell are listed in the p, i and n order respectively.

The main goal of using FDTD optimization was finding the right combinations of ZnO:Al height, radius and period that provide highest limiting current (minimum of the two photo-generated currents in the serial subcells) of the whole micromorph cell.

The optimization process of the IRL design was done by investigating different values in two subsequent steps. The first step investigated a broad range of values and the second one investigated more precise ones based on the results of the first steps.

The first step involved simulation of ZnO:Al heights from 0-40nm, radii from 0-300nm and periods from 0-1000nm. The ZnO:Al height positively affected the a-Si:H top current while the reverse is true for nc-Si:H bottom cell, this made the limiting current small for height of 0nm due to low nc-Si:H subcell and for height of 40nm due to low a-Si:H subcell (Figure 4-11). As for the radius, larger dimensions produce lower bottom cell generated current; this can be explained by the poor antireflection effect of large radius on short wavelengths. Lastly for the periods dimensions, large periods had a bad effect on the a-Si:H photo-generated current and small ones had bad effect on bottom nc-Si:H subcell which can be seen again from the color map graphs in Figure 4-11.

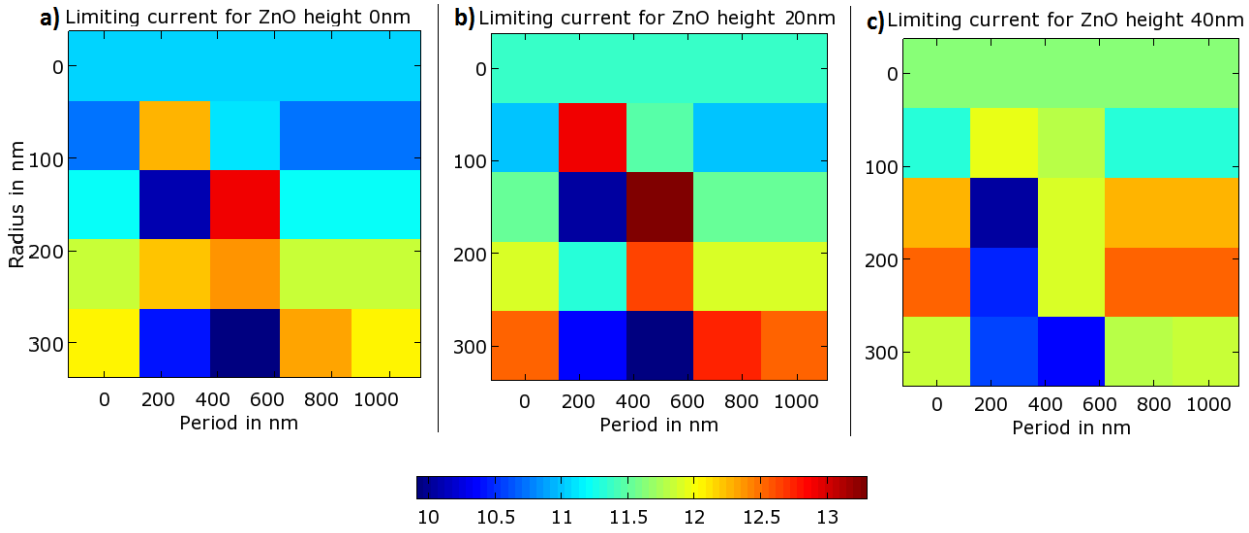

Figure 4-11, Jph (photo-generated current density in mA/cm^2) for different heights (a)0, b)20 and c)40nm) , radii from 0-300nm and periods from 0-1000nm.

The second simulations group studied photo-generated current density for heights from 15 to 30nm in 5nms increments, radii from 100-200nm and periods from 300-700nm (Figure 4-12). The best combinations produced a photocurrent density of 13.57 mA/cm^2 for a height of 30nm, radius of 100nm and a period of 330nm. The sweep analysis of the different dimensions was very close to the results obtained by the built-in optimization algorithm provided by the FDTD optimization package which produced 13.62 mA/cm^2 for a height of 25nm, radius of 120nm and a period of 330 nm.

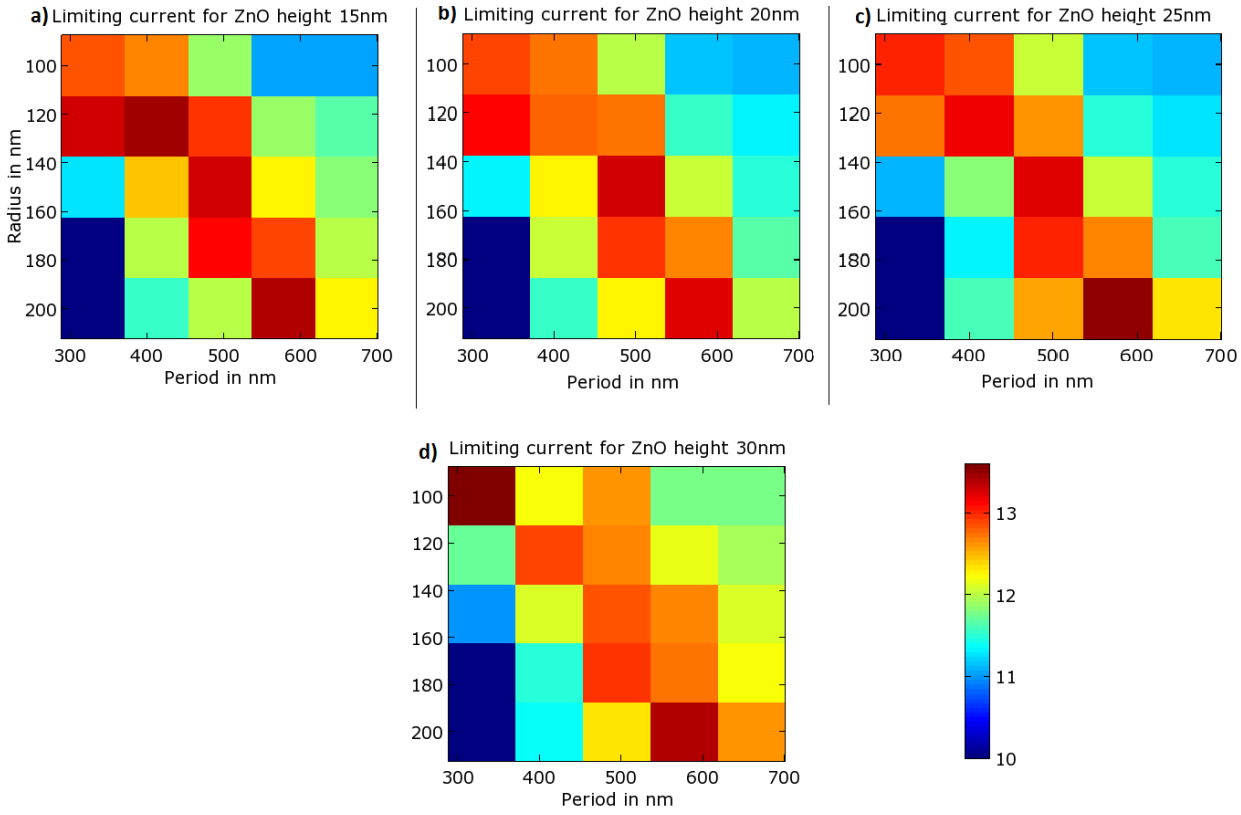

Figure 4-12, Jph (photo-generated current density in mA/cm^2) for different heights (a)15, b)20 , c)25nm and d)30nm) , radii from 100-200nm and periods from 300-700nm.

In Figure 4-13, the calculated power absorption density at different wavelengths is shown. At short wavelengths, the IRL reflects most of the light back to the top cell. As the wavelength increases, the IRL helps scatter the incident light to the bottom cell.

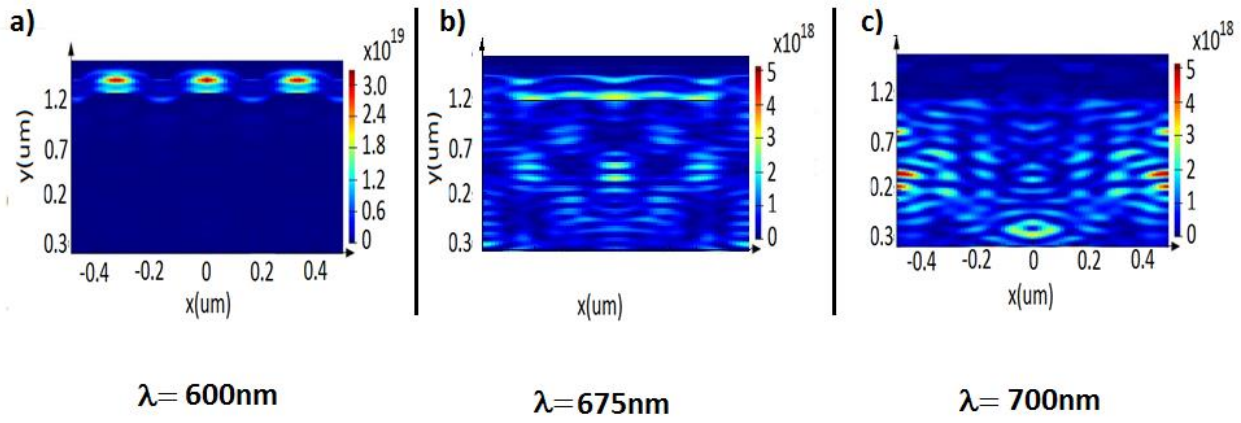

Figure 4-13, power absorption density for the micromorph structure at wavelengths 600, 675 and 700nm. Absorption is concentrated in the top a-Si:H cell for short wavelengths and in the bottom nc-Si:H subcell for long wavelengths.

4.2.1 Electrical simulation results

The optimized design comprises 3D features similar to other world record and other famous designs[71]; therefore, it is anticipated that electrical performance will be very close provided using same deposition techniques. Moreover, the design uses thinner layers and thus should have even better electrical performance. This was verified using 3D electrical simulation as detailed below.

3D photo-generated carrier profiles from AM1.5 sun irradiance (Figure 4-14 and Figure 4-15) were fed into the 3D device simulation package. Each subcell were simulated separately (n-i-p parts excluding ZnO:Al and substrate) and temperature used in the simulation was 300K and assumed constant. The values obtained are listed in Table 4-I while the complete J-V and power diagrams are shown in Figure 4-16.

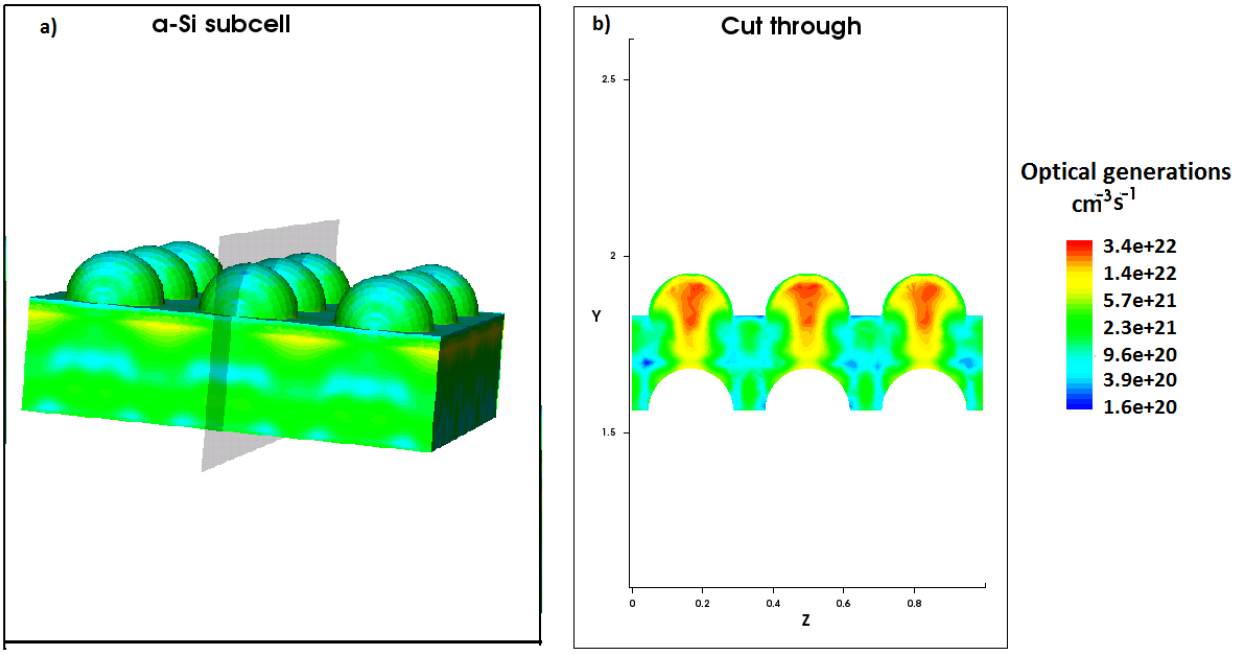

Figure 4-14, a) 3D photo-generated carrier profiles of the top as-Si:H subcell.B) 2D profile of a cut inside the cell.

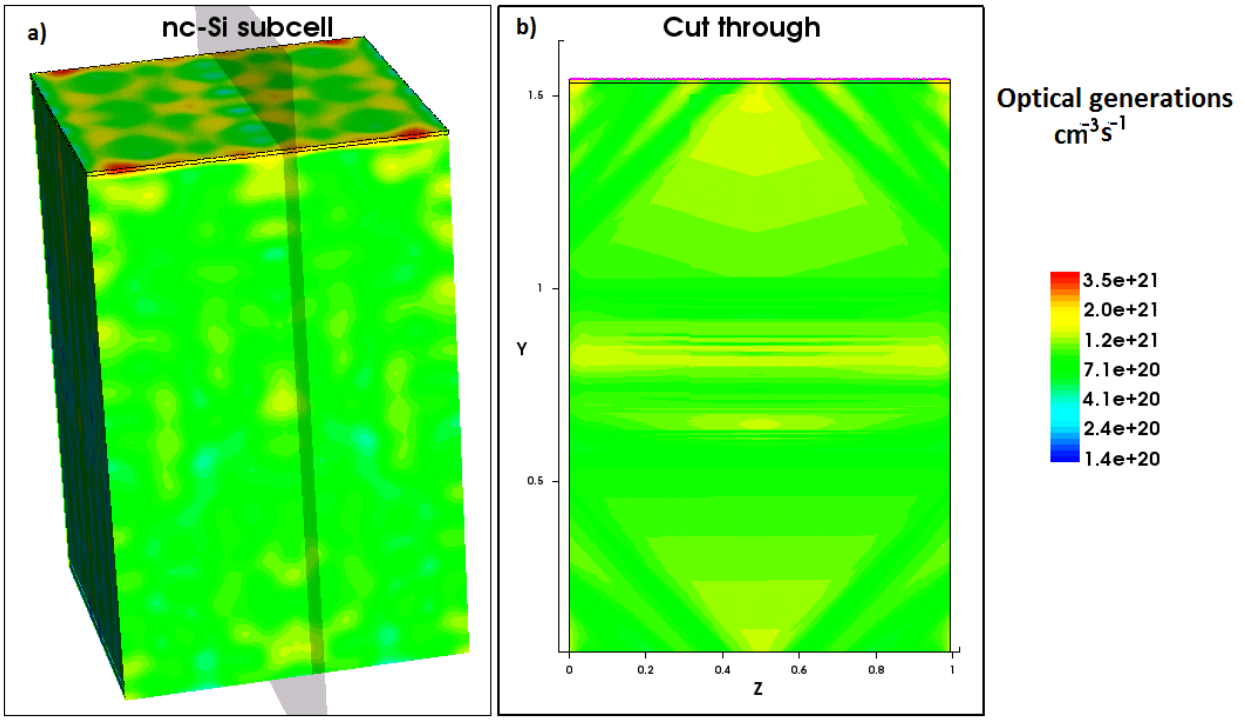

Figure 4-15, a) 3D photo-generated carrier profiles of the bottom nc-Si:H subcell.b) 2D profile of a cut inside the cell.

Table 4-I

Calculated open circuit voltage (V_{oc}), short-circuit current density (J_{sc}), Fill factor (FF) and max power (Pmax) of top and bottom subcells

Parameter	a-Si	nc-Si
V_{oc}(V)	0.97	0.49
J_{sc}(mA/cm^2)	13.69	12.96
FF	0.84	0.68
Pmax(mW/cm^2)	11.16	4.31

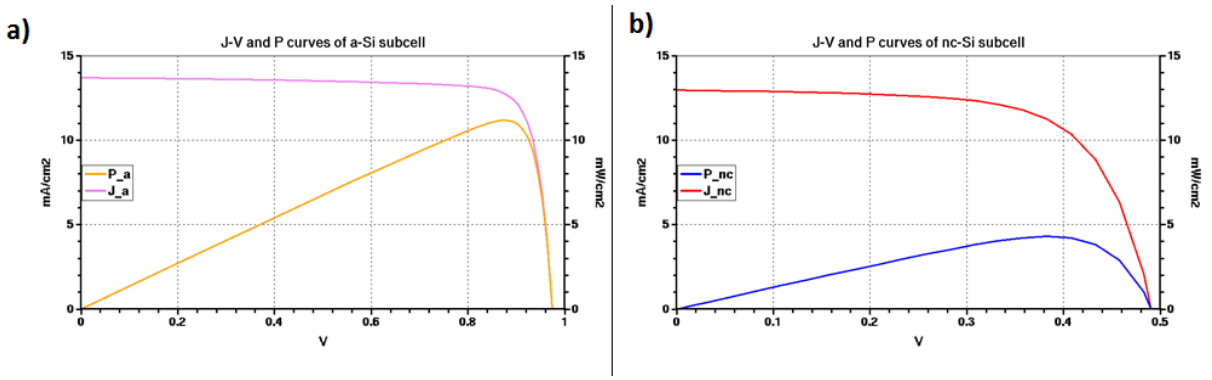

Figure 4-16, a) Illuminated current density(J) and Power density(P) over voltage of a-Si and b) nc-Sisubcells.

The sdevice input files used are shown in the appendix.

Although the above basic analysis suggests that the whole cell will be limited by the bottom subcell with 12.69 mA/cm^2 short circuit current density, it should be complemented by experimental calculation to recalculate the latter value after introducing serial resistances to account for the contacts.

The electrical results which also suggests a very good total V_{oc} of 1.46 (sum of two subcells) is very close to the current world record [5]. Experimental measurements should help conduct a second design iteration based on how close it is to the simulations results. For example, one can design the IRL such that the bottom subcell has an additional additional 0.7 mA/cm^2 photo-generated current to the upper subcell to achieve a higher short circuit current.

5 LOW-COST LITHOGRAPHY-FREE NANOTEXTURING OF MONOCRYSTALLINE SILICON

Developing solar cells with high efficiency and low cost are the ultimate goal of solar cell research. In this Chapter, a cheap texturing method is investigated experimentally and studied by FDTD simulation.

One of the main procedures in manufacturing high efficient silicon solar cells is increasing the Optical thickness of the silicon wafers enabling light to travel larger distances with the result of higher absorption. It is worth noting that that increasing optical thickness is accompanied by lowering bad antireflection properties of bare silicon. Realizing the above mentioned goals is often done by texturing the surface and/or adding antireflection coatings[17,72]. Recently, several nanostructures, both periodic and aperiodic, were studied experimentally and theoretically and showed very encouraging results, although many suffer from increased recombination of photo-generated carriers [73].

Nanostructures were fabricated by different techniques and have different levels of periodicity and dimensions control. Fabrication methods includes etching with it different subtypes (metal assisted, RIE, alkaline and acidic)[17,46,73] in addition to vapour–liquid–solid (VLS) growth and laser based Fabrication[73].

The experimental work in this part was done by the AUC Physics researcher and teaching assistant, AbdelAziz Goda, who is also a member of the Nanophotonics research laboratory, NRL, in the AUC.

My contribution was simulating the nanocones structures and providing guidance to what's the best dimension that provides greatest bulk absorption.

5.1 Fabrication of random nanocones on microcrystalline silicon wafers

Fabrication is based on a Metal assisted chemical etching (MACE) method used and published before and authored by AUC researcher Sara AbdelRazik in addition to Doctors

Mohamed Swillam and Nageh Allam[46]. The fabrication process produced vertically aligned and controlled Silicon Nanowires by first cleaning the wafer using multi processes then the cleaned pieces were submerged in an aqueous solution of silver nitrate and HFL acid at room temperature for 1 min. The last step involved removing the silver residues.

The new fabrication technique conducted by AbdelAziz involved reduced number of steps and produced nano textured silicon surfaces as shown in Figure 5-1.

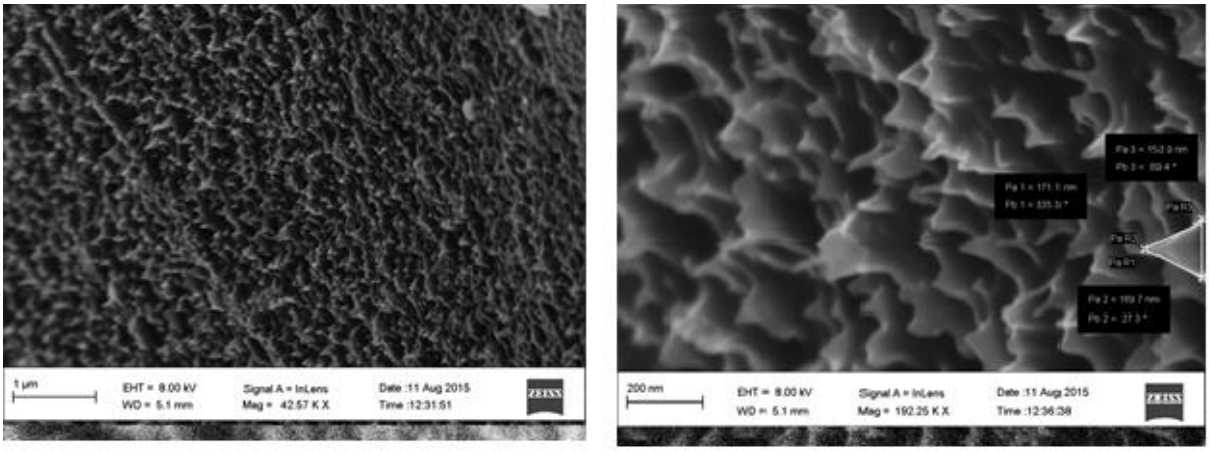

Figure 5-1, left figure shows a SEM graph of nano textured silicon surface. Right figure shows a zoomed-in SEM graph of the nanotextured surface featuring dimensions of one of the nanoconed shapes. Randomness can be seen.

Silicon nanocones were fabrication is illustrated in Figure 5-2. MACE is used to fabricate silicon nanowires (SiNWs). Wet or ambient oxidation of the MACE fabricated structure and subsequent etching of the oxidized SiNWs in 10 % HF as discussed in [74]. The sample is washed with DI water and finally dried with nitrogen. The concentration of the etchant solution (HF+H2O2), AgNO3, the etching time, and the temperature altogether control the etching rate and hence height and radius of SiNCs.

Figure 5-2, Schematic diagram of SiNCs fabrication steps.

Figure 5-3 show AFM (operating in tapping mode) image of the fabricated SiNCs array. Randomness in fabricated structure can be clearly seen and roughness statistics is also calculated. AFM data was exported to FDTD structure to simulate it, although simulation of the whole scanned area was not successful due to large memory requirements.

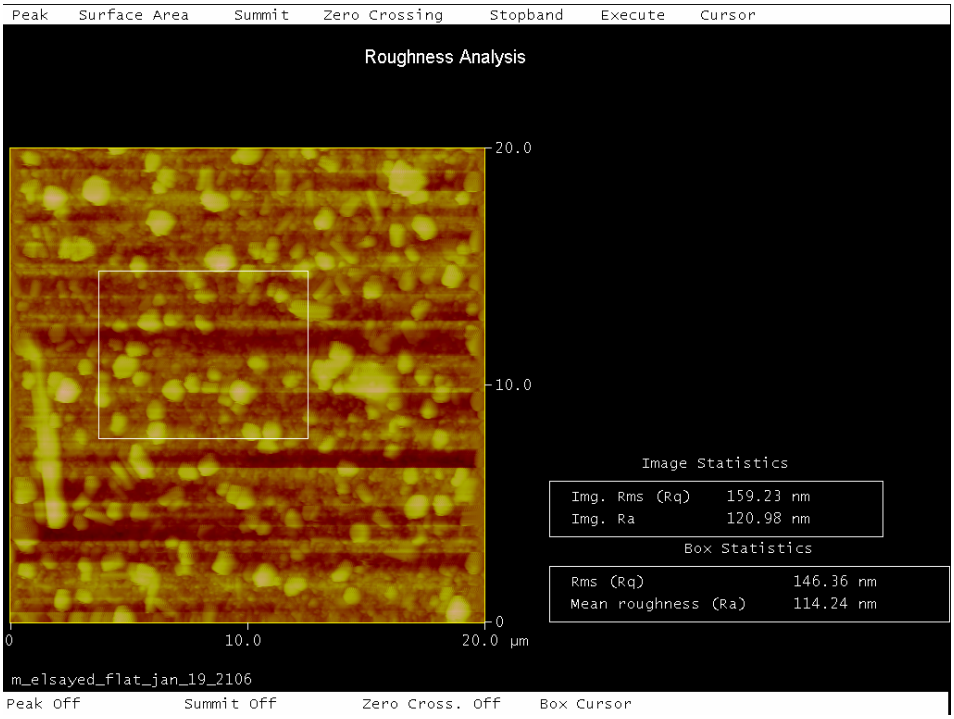

Figure 5-3, AFM image of random SiNCs array.

The effect of the nano texture on the antireflection properties were experimentally verified using a spectrophotometer and was proven to have much better antireflection properties in comparison to bare monocrystalline silicon (see Figure 5-4) .

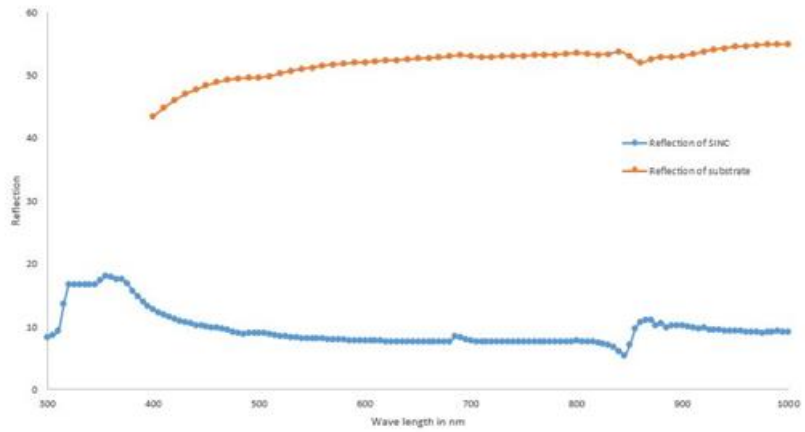

Figure 5-4, reflection properties of nanocone-like shapes and a bare substrate as measured by a spectrophotometer.

5.2 FDTD analysis and study of nanocone shapes

The fabricated nanotextures was modelled by a periodic nanocone on top of a silicon wafer with a height of 150nm, period and radius are 0.36 and 0.18 respectively as shown in Figure 5-5.

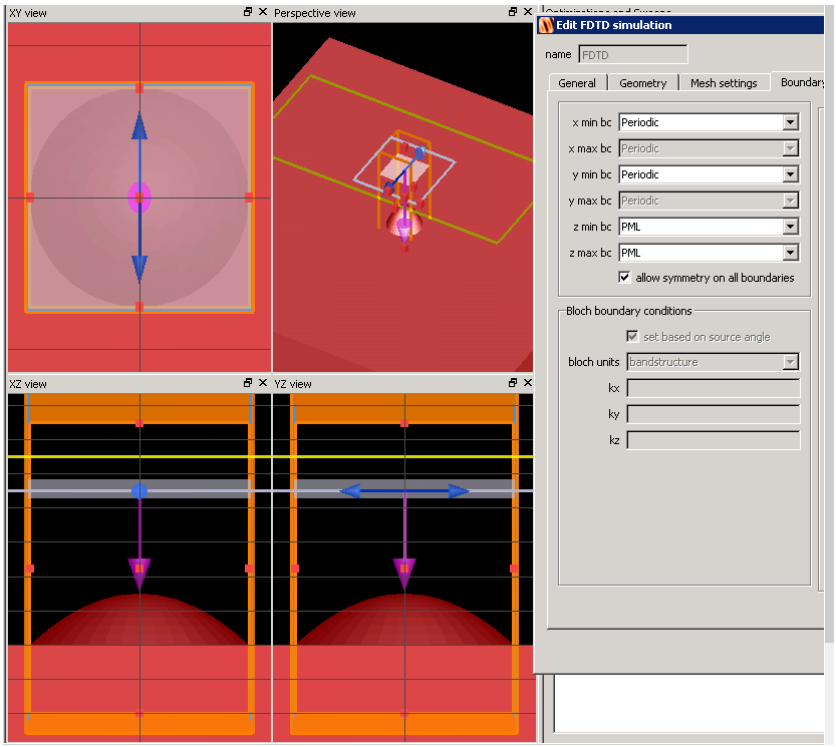

Figure 5-5, Lumerical screenshots of the simulated structure. Simulated area is one nanocone with periodic boundary conditions.

The simulation assessed both the dimensions and tolerance of fabricated structures. To compare the fabricated results with dimensions that produce the optimal antireflection properties with best bulk absorption, the optimization feature of the Lumerical package was used and a wide range of heights (0.1-0.2 um), radius (0.1-0.5um) and periods (0.2-1um) were investigated and the optimized dimensions were height of 0.2um, radius 0.1 and period 0.2 which is very close to the fabricated dimensions and provided very close results as shown in Figure 5-6.

Simulation provided guidance that fabrication dimensions requirements are well tolerated and this can be attributed to the nanocones structures that provide gradual increase in refractive index.

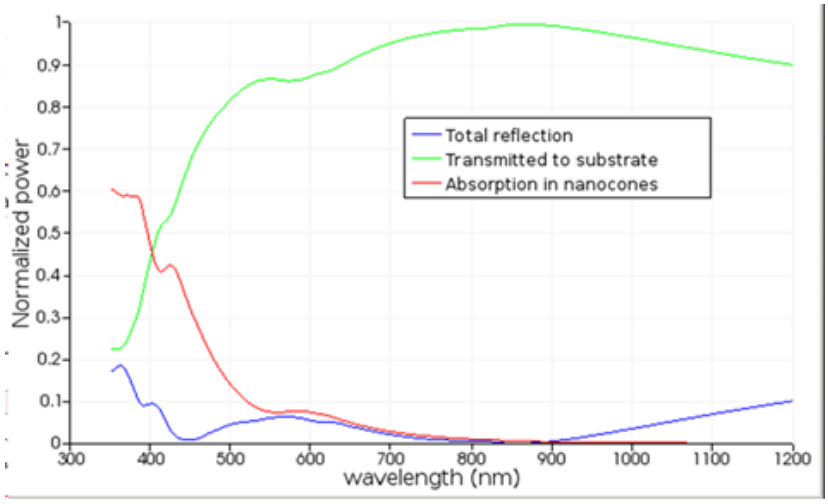

Figure 5-6, shows total reflection, power absorbed to the substrate and the absorption in optimized nanocones.

The experimental results differed from the experimental ones due to the randomness of the structure and formation of a top oxide layer. This was verified by simulating a random texture with a size of 2um * 2um and root mean square height of 200nm and correlation lengths in the x and y directions of 200nm in addition to a top oxide layer of thickness 100nm which produced very close results (see Figure 5-7).

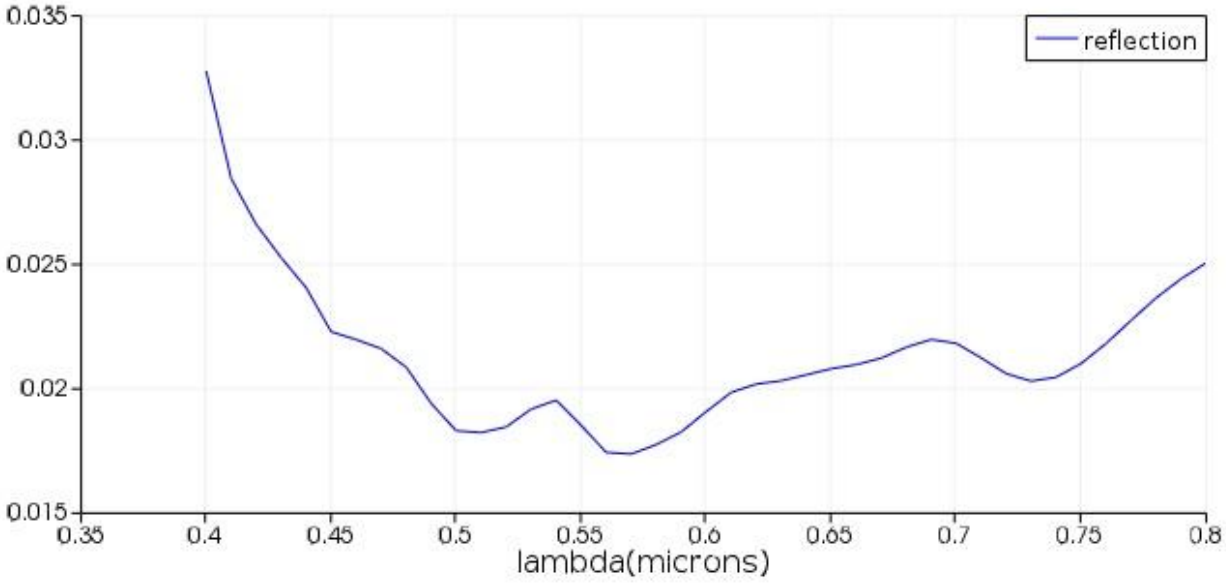

Figure 5-7, reflection spectrum of a random texture with a size of 2um * 2um and rms height of 200nm and correlation lengths in the x and y directions of 200nm in addition to a top oxide layer of thickness 100nm.

Finally, to further study the effect of the angle of incidence on the antireflection properties, experimental measures of the nanocones were performed with different incident angles as shown in **Error! Reference source not found.**. **Error! Reference source not found.** (a) and (b) compare the reflection of SiNCs array and bare Si measured at different angles from 400 nm to 800 nm wavelength range.

Generally, the reflectance is directly proportional to incident angle. Our fabricated SiNCs produced enhanced antireflection properties compared to earlier reported nanostructures[72,74].

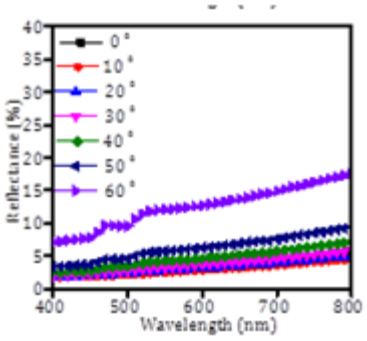

Figure 5-8, Experimental reflectance for incident angles from 0-60^{o} for the fabricated SiNCs array.

6 CONCLUSIONS AND FUTURE WORK

Solar energy harvesting and related applications such as water desalination are core technologies that enable humanity to live a prosper future. Photovoltaics is a promising solar energy harvesting method and Silicon, whether crystalline or amorphous, dominates the technology from decades and has many reasons to stay the dominant technology for other decades to come.

In this thesis, low-cost and CMOS compatible plasmonic TiN was studied in many realizations of thin-film and crystalline silicon solar cells. FDTD Optimized back plasmonic TiN structures showed a comparable and very close enhancement effect to that of silver with same structures. The CMOS compatibility and great cost reduction in using TiN as a replacement for silver, in addition to its abundance and ease of fabrication, make it a very promising alternative in plasmonic solar cell applications.

It is worth noting that electrical performance still needs to be studied. Finally, fabrication challenges like oxidation of TiN and relative high resistivity should be examined.

In design 2, a novel IRL optical design is conceptually demonstrated and produced a very promising simulation. The advantage of the proposed design is the degree of freedom in choosing hemispheres dimensions to suit design spectral requirements of the IRL which make the design applicable to diverse types of solar cells.

At last, random textured SiNCs array were fabricated through MACE and oxidation in addition to theoretically studying the effect of dimensions on the facial antireflection properties. The simple low-cost controllable method shows a very promising broadband antireflective property to normal and oblique incident light. This antireflection property is due to the gradual change in the effective front refractive index of the structure and its "roughness". The proposed SiNCs array can be used in a range of fields in addition to photovoltaics such as biosensing, electronic and optoelectronic applications.

SiNWs and SiNCs have been studied extensively by many researchers, especially during the past decade; however, the reported efficiencies have stayed far lower than relatively traditional cells. Breakthroughs in the manufacturing and understanding of these devices are needed.

6.1 Possible future works:

1. Experimental work should be conducted to verify the optical simulation and basic electrical analysis of TiN plasmonic structures.
2. Other periodic IRL designs should be studied.
3. Realization of complete PN junctions in the SiNCs. This has many challenges:
    a. Passivation of the large areas introduced by SiNCs to improve electrical properties.
    b. Studying radial and other types of junctions and figuring a way for the complex fabrication requirements and challenging electrical performance consequences.
4. Studying forming SiNWs and/or other silicon nanostructures from different active or antireflection materials.

7 APPENDIX

7.1 Mesh transformation MATLAB script

```
% Modified by Ahmed Emad to do 3D mapping.
% Original code and whole thesis of the original author can be downloaded
%from
% http://hypnos.caltech.edu/~mkelzenb/thesis.html
%%%%%%%%%%%%%%%%%%%%%%%%%%%%%%%%%%%%%%%%%%%%%%%%%%%%%%%%%%%%%%%%%%%%%%%%%%%%
%%%
%Permission to reproduce the code was provided by Michael Kelzenberg
% MATLAB script for importing arbitrary profiles onto DF-ISE simulation
% grids for use with Sentaurus TCAD.
%
% Michael Kelzenberg, 2010
%
% This script reads a DF-ISE .dat file to determine the spatial coordinates
%of
% of each grid point.  It then generates a new .dat file containing an
% OpticalGeneration profile that was calculated by FDTD.  The key
input/output
% settings and the mapping function are indicated by comments in the code.
%%%%%%%%%%%%%%%%%%%%%%%%%%%%%%%%%%%%%%%%%%%%%%%%%%%%%%%%%%%%%%%%%%%%%%%%%%%%
%%%

%DAT file
%%%%%%%%%%%%%%%%%%%%%%%%%%%%%%%%%%%%%%%%%%%%%%%%%%%%%%%%%%%%%%%%%%%%%%%%%%%%
%%%
%This should be a valid DF-ISE .dat file (i.e. generated by mesh or
%noffset3d.  The meshing program must be scripted to store the x, y and z
%position of each vertex of the grid as "PMIUserField0","PMIUserField1" and
%"PMIUserField2", respectively.
%%%%%%%%%%%%%%%%%%%%%%%%%%%%%%%%%%%%%%%%%%%%%%%%%%%%%%%%%%%%%%%%%%%%%%%%%%%%
%%%

datFile = 'IRLas-Mar27.dat';
grdFile = 'IRLas-Mar27.grd';

%FDTD MAT file
%%%%%%%%%%%%%%%%%%%%%%%%%%%%%%%%%%%%%%%%%%%%%%%%%%%%%%%%%%%%%%%%%%%%%%%%%%%%
%This is the Matlab MAT file generated by the Lumericalsimulation
%including:
% x,y,z     X, Y and Z  specification of grid (m)
% G         Matrix of optical generation rate (per cm3 per s)
%%%%%%%%%%%%%%%%%%%%%%%%%%%%%%%%%%%%%%%%%%%%%%%%%%%%%%%%%%%%%%%%%%%%%%%%%%%%
%%%

FDTDFile = 'Gall-Inter-D.mat';

%Regions to process
%%%%%%%%%%%%%%%%%%%%%%%%%%%%%%%%%%%%%%%%%%%%%%%%%%%%%%%%%%%%%%%%%%%%%%%%%%%%
%These are the regions to perform the optical generation mesh conversion.
```

```
%This must be a cell array of region names, including double-quotes (")
%around each region name!!!
%  Example syntax: regionsToProcess = {'"Base_region"', "Emitter_region"' };
%%%%%%%%%%%%%%%%%%%%%%%%%%%%%%%%%%%%%%%%%%%%%%%%%%%%%%%%%%%%%%%%%%%%%%%%%%%%%%%%
%%%
%regionsToProcess = {'"region_2"'};
regionsToProcess = {'"region_asi_b0"' '"region_asi_b1"' '"region_asi_b2"'
'"region_asi_b3"'  '"region_asi_b4"' '"region_asi_b5"' '"region_asi_b6"'
'"region_asi_b7"' '"region_asi_b8"'  '"region_asi_b9"' '"region_asin"'
'"region_asip_b0"' '"region_asin_lump_2_b1"' '"region_asip_b1"'
'"region_asin_lump_2_b2"'    '"region_asip_b2"' '"region_asin_lump_2_b3"'
'"region_asip_b3"' '"region_asin_lump_2_b4"' '"region_asip_b4"'
'"region_asin_lump_2_b5"' '"region_asip_b5"' '"region_asin_lump_2_b6"'
'"region_asip_b6"'  '"region_asin_lump_2_b7"' '"region_asip_b7"'
'"region_asin_lump_2_b8"' '"region_asip_b8"'  '"region_asin_lump_2_b0"'
'"region_asip_b9"'};
%The output dat and grd files are used for device  physics simulations
outputFile = ['Opti-as-Mar.dat'];
outputGrid = ['Opti-as-Mar.grd'];


%Number of data values to output per line in output DAT file
numperline = 10;


disp('');
disp('------------------------------------------------------------------');
disp(['OptGenConverter Version 2']);
disp(['(c) 2010 Michael Kelzenberg']);
disp(['California Institute of Technology']);
disp('------------------------------------------------------------------');
disp(' ');


disp(['Opening DAT file ' datFile ]);

grd = fopen(datFile);
if (grd < 1)
    error(['Error opening file ' datFile ' for reading.']);
    %exit
end

if ( ~isequal( fgetl(grd), 'DF-ISE text'))
    disp('Error with grid file format: It might not be a DF_ISE text file.');
    disp('Please double-check input file.  The first line should read:');
    disp('     DF-ISE text');
    error('File parse error');

end
fln = 1;

verts = [];
regions = {};

nl = fgetl(grd); fln=fln+1;
```

```
while( isempty( regexp(nl, 'nb_vertices *= *[0-9]+') ) && ~feof(grd) )
    nl = fgetl(grd); fln=fln+1;
end
tmp=regexp(nl, '[0-9]+','match');
numverts = str2num(tmp{1});
disp(['  File reports ' num2str(numverts) ' vertices']);

nl = fgetl(grd); fln=fln+1;
while( isempty( regexp(nl, 'nb_edges *= *[0-9]+') ) && ~feof(grd) )
    nl = fgetl(grd); fln=fln+1;
end
tmp=regexp(nl, '[0-9]+','match');
numedges = str2num(tmp{1});
disp(['  File reports ' num2str(numedges) ' edges']);

nl = fgetl(grd); fln=fln+1;
while( isempty( regexp(nl, 'nb_elements *= *[0-9]+') ) && ~feof(grd) )
    nl = fgetl(grd); fln=fln+1;
end
tmp=regexp(nl, '[0-9]+','match');
numelems = str2num(tmp{1});
disp(['  File reports ' num2str(numelems) ' elements']);

nl = fgetl(grd); fln=fln+1;
while( isempty( regexp(nl, 'nb_regions *= *[0-9]+') ) && ~feof(grd) )
    nl = fgetl(grd); fln=fln+1;
end
tmp = regexp(nl, '[0-9]+','match');
numregions = str2num(tmp{1});
disp(['  File reports ' num2str(numregions) ' regions']);

%Advance to data section of file...
nl = fgetl(grd); fln=fln+1;
while( isempty( regexp(nl, 'Data.*\{', 'once') ) && ~feof(grd) )
    nl = fgetl(grd); fln=fln+1;
end

if ( feof(grd) )
    disp('Unexpected end-of-file, no data processed.');
    disp(['Line: ' num2str(fln)]);
    error('File parse error.');
end


regionArray = [];
disp(' ');
disp('Reading data points...');
%Main reading loop.  Look for PMIUserField 0, 1 and 2 data sets...
while ~feof(grd)

    nl = fgetl(grd); fln=fln+1;
    while ( isempty(
regexpi(nl,'\s*function\s*=\s*PMIUserField[012]','once'))...
            && ~feof(grd) )
        nl = fgetl(grd); fln=fln+1;
```

```
    end
    if (feof(grd))
        break
    end

    tmp = regexp(nl, '[012]','match');
    axisNumber = str2num(tmp{1});

    nl = fgetl(grd); fln=fln+1;
    while ( isempty( regexpi(nl, '\s*validity\s*=\s*\[\s*".*"\s*\]',
'once'))...
            && ~feof(grd) )
        nl = fgetl(grd); fln=fln+1;
    end

    if (feof(grd))
        error(['File Parse Error near line ' num2str(fln)]);
        break
    end
    tmp = regexp(nl, '".*"','match');
    regionName = tmp{1};

    nl = fgetl(grd); fln=fln+1;
    while ( isempty( regexpi(nl, '\s*Values\s*\(\s*[0-9]+\s*\)', 'once') )...
            && ~feof(grd) )
        nl = fgetl(grd); fln=fln+1;
    end

    if (feof(grd))
        disp(['File Parse Error near line ' num2str(fln)]);
        break
    end
    tmp = regexp(nl, '[0-9]+','match');
    numElems = str2num(tmp{1});

    dataPoints = [];
    while (1)
        nl = fgetl(grd); fln = fln+1;
        if(isempty(regexp(nl,'[0-9]+') ) )
            break
        else
            thisline = regexp(nl,'[\.\-\e\E\+0-9][\s\.\-\e\E\+0-
9]*','match');
            thisline = thisline{1};
            dataPoints = [dataPoints str2num(thisline)];
        end
        if ( ~isempty(regexp(nl,'}','once') ))
            break
        end
    end

    disp(['  Region ' regionName ' read ' num2str(length(dataPoints)) '/' ...
        num2str(numElems) ' elements for axis ' num2str(axisNumber) ]);

    %Error if data points disagree with number stated in header
```

```
    if ( numElems ~= length(dataPoints) )
        disp(['Error: number of data points does not match file header']);
        disp(['Parse error near line ' num2str(fln)]);
        error(['File structure error in region ' regionName]);
    end

    existingRegion = 0;
    for n=1:length(regionArray)
        canRegion = regionArray{n};
        if (isequal(regionName,canRegion.name))
            existingRegion = n;
        end
    end

    if (existingRegion)
        if (axisNumber == 0)
            regionArray{existingRegion}.xdata = dataPoints;
        elseif (axisNumber == 1)
            regionArray{existingRegion}.ydata = dataPoints;
        else
            regionArray{existingRegion}.zdata = dataPoints;
        end

        if ~isequal( length(regionArray{existingRegion}.xdata), ...
                length(regionArray{existingRegion}.ydata) )
            disp(['Error: number of x data points does not match number of '
...
                    'y data points']);
            error(['File structure error in region ' regionName ]);
        end

    else
        newRegion.name = regionName;
        if (axisNumber == 0)
            newRegion.xdata = dataPoints;
            newRegion.ydata = [];
            newRegion.zdata = [];
        elseif (axisNumber == 1)
            newRegion.ydata = dataPoints;
            newRegion.xdata = [];
            newRegion.zdata = [];
        else
             newRegion.xdata = [];
              newRegion.ydata = [];
            newRegion.zdata = dataPoints;
        end
    newRegion.gdata = zeros(size(dataPoints));
        regionArray{end+1} = newRegion;
    end

end

for n=1:length(regionArray)
    if ~isequal( length(regionArray{n}.xdata), length(regionArray{n}.ydata) )
            disp(['Error: number of x data points does not match number of
'...
```

```
                'y data points']);
            error(['File structure error in region ' regionArray{n}.name ]);
    end
end

disp(' ');
disp('Completed reading DAT file');
disp(['  Read ' num2str(length(regionArray)) ' region(s)']);
disp(' ');
fclose(grd);

%Now ensure that data was successfully read for all requested regions
regionsToProcess = unique(regionsToProcess);
for n=1:length(regionsToProcess)
    reqName = regionsToProcess{n};
    hasRegion = 0;
    for m=1:length(regionArray)
        if isequal( reqName, regionArray{m}.name )
             hasRegion=1;
        break;
        end
    end
    if ~hasRegion
        disp(['Error: Vertex position information for requested region ' ...
            reqName ' not contained within this grid.']);
        error(['Unable to process region: ' reqName ]);
    end
end

% We're done parsing grid file -- Now we load FDTD results and define the
% mapping function.  Note that the spatial translation applied to the x, y
% and z-coordinates in the mapping function is specific to the project
geometry:
disp(' ');
disp(['Loading MAT file ' FDTDFile ]);
load(FDTDFile);
optGenMatrix = G;
%%%%%%%%%%%%%%%%%%%%%%%%%%%%%%%%%%%%%%%%%%%%%%%%%%%%%%%%%%%%%%%%%%%%%%%%%%%%%
%%%
%Mapping function:
newoptgen = @(xi, yi, zi) interpn(x,y,z, optGenMatrix, xi,yi,zi,'linear',0);
%%%%%%%%%%%%%%%%%%%%%%%%%%%%%%%%%%%%%%%%%%%%%%%%%%%%%%%%%%%%%%%%%%%%%%%%%%%%%
%%%

% Now ready to write the output data file...
disp(['Opening output file ' outputFile ]);

ogo = fopen(outputFile,'w');
if (ogo < 1)
    error(['Error opening file ' outputFile ' for writing.']);
end

fprintf(ogo, 'DF-ISE text\n\n');
fprintf(ogo, ...
   'Info {\n  version     = 1.0\n  type        = dataset\n  dimension   =
2\n');
```

```
fprintf(ogo, '  nb_vertices = %d\n  nb_edges    = %d\n  nb_faces    =
0\n',...
    numverts, numedges);
fprintf(ogo, '  nb_elements = %d\n  nb_regions  = %d\n  datasets    = [ ',...
    numelems, numregions);
for n=1:length(regionsToProcess)
    fprintf(ogo,'"OpticalGeneration" ');
end
fprintf(ogo, ']\n  functions   = [ ');
    for n=1:length(regionsToProcess)
        fprintf(ogo,'OpticalGeneration ');
    end
fprintf(ogo, ']\n}\n\nData {\n\n');

for n=1:length(regionsToProcess)
    reqName = regionsToProcess{n};
    hasRegion = 0;
    for m=1:length(regionArray)
        if isequal( reqName, regionArray{m}.name )
            hasRegion=m;
            break;
        end
    end
    if (hasRegion)
        reg = regionArray{hasRegion};

        disp( ['Proessing Optical Generation for region ' reg.name '...'] );

        fprintf(ogo,['Dataset ("OpticalGeneration") {\n  function  = '...
            'OpticalGeneration\n  type      = scalar\n  dimension = 1\n'...
            'location  = vertex\n  validity  = [ ' reg.name ' ]\n' ] );
        fprintf(ogo, '  Values (%d) {\n', length(reg.xdata) );

        % this part was added to substract 10e-12 m from each coordinate
        % value to fix an error in the 3D interpolation function.
    gdata = zeros(size(reg.xdata));
        nl = 1;
        for nv=1:length(reg.xdata)
            if(reg.xdata(nv))
            reg.xdata(nv)=reg.xdata(nv)-.000001
            end
            if(reg.ydata(nv))
            reg.ydata(nv)=reg.ydata(nv)-.000001
            end
            if(reg.zdata(nv))
            reg.zdata(nv)=reg.zdata(nv)-.000001
            end
            ogi = newoptgen(reg.xdata(nv), reg.ydata(nv),reg.zdata(nv));
            if (ogi == 0)
                disp([reg.xdata(nv),reg.ydata(nv),reg.zdata(nv)]);
            end


            %%Ahmed
            fprintf(ogo, ' %22e', ogi);
        gdata(nv) = ogi;
```

```
            nl = nl + 1;
            if (nl > 10)
                fprintf(ogo, '\n');
                nl = 1;
            end
        end
        if (nl > 1)
            fprintf(ogo,'\n');
        end
        fprintf(ogo, '  }\n}\n\n');

        disp( ['   ' num2str(length(reg.xdata))  ' processed'] );
        regionArray{hasRegion}.gdata = gdata;

    end

 end

fprintf(ogo,'\n\n}');
fclose(ogo);
disp(['Finished writing output file ' outputFile ]);

disp(' ');
disp(['Copying from grid file: ' grdFile]);
copyfile(grdFile,outputGrid);
disp(['To grid file: ' outputGrid]);
```

7.2 Top cell Sentarus SDEVICE file

```
File{
   Grid      = "IRL-asonly3.tdr"
   Parameter = "IRL-models-as-May.par"
   OpticalGenerationInput= "IRL-asonly3Opti.tdr"
   Plot      = "IRL-as-May-ohm"
   Current   = "IRL-as-May-ohm"
   Output    = "3IRL-as-May-ohm"
}

Electrode{
   { Name="top"    Voltage=0.0 }
   { Name="bottom"    Voltage=0.0 }
}

Physics (Material="aSip"){

Traps(
(eNeutral Exponential fromCondBand Conc=1e21 EnergyMid=0
EnergySig=0.06 eXsection=1e-17 hXsection=1e-15)

(hNeutral Exponential  fromValBand Conc=1e21 EnergyMid=0 EnergySig=0.1
eXsection=1e-17 hXsection=1e-15)

(hNeutral Gaussian fromCondBand Conc=1e18 EnergyMid=0.7 EnergySig=0.15
eXsection=1e-15 hXsection=1e-16)
(hNeutral Gaussian fromCondBand Conc=1e18 EnergyMid=1.27
EnergySig=0.08 eXsection=1e-15 hXsection=1e-16)
(eNeutral Gaussian fromValBand Conc=1e16 EnergyMid=1.17 EnergySig=0.08
eXsection=1e-17 hXsection=1e-15) )
}

Physics (Material="aSi"){


Traps(
(eNeutral Exponential fromCondBand Conc=1e21 EnergyMid=0
EnergySig=0.02 eXsection=1e-15 hXsection=1e-17)
 (hNeutral Exponential fromValBand Conc=1e21 EnergyMid=0
EnergySig=0.05 eXsection=1e-17 hXsection=1e-15)

(hNeutral Gaussian fromCondBand Conc=4e15 EnergyMid=0.56
EnergySig=0.06 eXsection=1e-15 hXsection=1e-16)
(hNeutral Gaussian fromCondBand Conc=4e15 EnergyMid=0.9 EnergySig=0.06
eXsection=1e-15 hXsection=1e-16)
(eNeutral Gaussian fromValBand Conc=4e15 EnergyMid=0.7 EnergySig=0.06
eXsection=1e-17 hXsection=1e-15) )

}
```

```
Physics (Material="aSin"){
Traps(
(eNeutral Exponential fromCondBand Conc=1e21 EnergyMid=0
EnergySig=0.04 eXsection=1e-15 hXsection=1e-17)
 (hNeutral Exponential fromValBand Conc=1e21 EnergyMid=0
EnergySig=0.06 eXsection=1e-17 hXsection=1e-15)

(hNeutral Gaussian fromCondBand Conc=1e16 EnergyMid=1.2 EnergySig=0.08
eXsection=1e-15 hXsection=1e-16)
(eNeutral Gaussian fromValBand Conc=1e16 EnergyMid=1.24 EnergySig=0.08
eXsection=1e-15 hXsection=1e-16)
(eNeutral Gaussian fromValBand Conc=4e18 EnergyMid=0.8 EnergySig=0.15
eXsection=1e-17 hXsection=1e-15) )
}

Physics{
   * DriftDiffusion
*AreaFactor = 5e10 * 1e11/w
 Optics(
    OpticalGeneration(
      ReadFromFile(
)
)
)



}

Plot{
*--Density and Currents, etc
   eDensity hDensity
   TotalCurrent/Vector eCurrent/Vector hCurrent/Vector
   eMobility hMobility
   eVelocity hVelocity
   eQuasiFermi hQuasiFermi

*--Temperature
   eTemperature Temperature * hTemperature

*--Fields and charges
   ElectricField/Vector Potential SpaceCharge

*--Doping Profiles
   Doping DonorConcentration AcceptorConcentration



*--Driving forces
   eGradQuasiFermi/Vector hGradQuasiFermi/Vector
   eEparallel hEparallel eENormal hENormal
```

```
*--Band structure/Composition
   BandGap
   Affinity
   ConductionBand ValenceBand
   eTrappedCharge hTrappedCharge
   eGapStatesRecombination hGapStatesRecombination TotalRecombination
*--Generation
OpticalGeneration
}

Math {
   Extrapolate
   Iterations=50
   Notdamped =100
   RelErrControl
   Number_of_Threads = 20

}

Solve {
   Coupled (Iterations=120) { poisson }
 Coupled (Iterations=120) { poisson electron hole }
NewCurrentPrefix="IV"


  Quasistationary (
      InitialStep=0.01 MaxStep =0.2 MinStep = 1e-7
      Goal{ Name= "top" Voltage=0.8}
 ){
      Coupled {Poisson Electron Hole}
  }
   Quasistationary (
      InitialStep=0.01 MaxStep =0.05 MinStep = 1e-7
      Goal{ Name= "top" Voltage=1}
 ){
      Coupled {Poisson Electron Hole}
  }
}
```

7.3 Bottom cell Sentarus SDEVICE file

```
File{
   Grid      = "IRL-nc3.tdr"
   Parameter = "IRL-nc-models.par"
   OpticalGenerationInput= "IRL-nc3Opti.tdr"
   Plot      = "IRL-ncMay-sen"
   Current   = "IRL-ncMay-sen"
   Output    = "3IRL-ncMay-sen"
}

Electrode{
   { Name="top"    Voltage=0.0 }
   { Name="bottom"    Voltage=0.0 }
}


Physics (Material="nc_Sip"){

Traps(

(eNeutral Gaussian fromMidBandGap Conc=3.5e17 EnergyMid=0.1
EnergySig=0.15 eXsection=1e-16 hXsection=1e-14)
(hNeutral Gaussian fromMidBandGap Conc=3.5e17 EnergyMid=-0.1
EnergySig=0.15 eXsection=1e-14 hXsection=1e-16)
)
}

Physics (Material="nc_Si"){

Traps(

(eNeutral Gaussian fromMidBandGap Conc=3.5e15 EnergyMid=0.1
EnergySig=0.15 eXsection=1e-16 hXsection=1e-14)
(hNeutral Gaussian fromMidBandGap Conc=3.5e15 EnergyMid=-0.1
EnergySig=0.15 eXsection=1e-14 hXsection=1e-16)
)
}

Physics (Material="nc_Sin"){
Traps(

(eNeutral Gaussian fromMidBandGap Conc=3.5e17 EnergyMid=0.1
EnergySig=0.2 eXsection=1e-16 hXsection=1e-14)
(hNeutral Gaussian fromMidBandGap Conc=3.5e17 EnergyMid=-0.1
EnergySig=0.2 eXsection=1e-14 hXsection=1e-16)

)
}
```

```
Physics{
   * DriftDiffusion
*AreaFactor = 5e10 * 1e11/w
 Optics(
    OpticalGeneration(
      ReadFromFile(
)
)
)



}

Plot{
*--Density and Currents, etc
   eDensity hDensity
   TotalCurrent/Vector eCurrent/Vector hCurrent/Vector
   eMobility hMobility
   eVelocity hVelocity
   eQuasiFermi hQuasiFermi

*--Temperature
   eTemperature Temperature * hTemperature

*--Fields and charges
   ElectricField/Vector Potential SpaceCharge

*--Doping Profiles
   Doping DonorConcentration AcceptorConcentration



*--Driving forces
   eGradQuasiFermi/Vector hGradQuasiFermi/Vector
   eEparallel hEparallel eENormal hENormal

*--Band structure/Composition
   BandGap
   Affinity
   ConductionBand ValenceBand
   eTrappedCharge hTrappedCharge
   eGapStatesRecombination hGapStatesRecombination TotalRecombination
*--Generation
OpticalGeneration
}
```

```
Math {
   Extrapolate
   Iterations=20
   Notdamped =100
   RelErrControl
   Number_of_Threads = 30

}

Solve {
   Coupled (Iterations=100) { poisson }
 Coupled (Iterations=100) { poisson electron hole }
NewCurrentPrefix="IV"

   Quasistationary (
      InitialStep=0.01 MaxStep =0.05 MinStep = 1e-7
      Goal{ Name= "top" Voltage=0.5}
 ){
      Coupled {Poisson Electron Hole}
  }

}
```

REFERENCES

1. N. S. Lewis and G. Crabtree, "Basic Research Needs for Solar Energy Utilization: report of the Basic Energy Sciences Workshop on Solar Energy Utilization, April 18-21, 2005," (2005).

2. N. S. Lewis, "Toward cost-effective solar energy use," Science **315,** 798-801 (2007).

3. S. Fonash, *Solar cell device physics* (Elsevier, 2012).

4. O. ISABELLA, "**Light management in thin-film silicon solar cells**," (2013).

5. M. A. Green, K. Emery, Y. Hishikawa, W. Warta, and E. D. Dunlop, "Solar cell efficiency tables (version 44)," Prog Photovoltaics Res Appl **22,** 701-710 (2014).

6. M. A. Green, *Third generation photovoltaics: advanced solar energy conversion* (Springer, 2006).

7. A. Polman and H. A. Atwater, "Photonic design principles for ultrahigh-efficiency photovoltaics," Nature materials **11,** 174-177 (2012).

8. W. Shockley and H. J. Queisser, "Detailed balance limit of efficiency of p-n junction solar cells," J. Appl. Phys. **32,** 510-519 (1961).

9. Anonymous "**Rare Earth Elements—Critical Resources for High Technology**," http://pubs.usgs.gov/fs/2002/fs087-02/.

10. R. Collins, A. Ferlauto, G. Ferreira, C. Chen, J. Koh, R. Koval, Y. Lee, J. Pearce, and C. Wronski, "Evolution of microstructure and phase in amorphous, protocrystalline, and microcrystalline silicon studied by real time spectroscopic ellipsometry," Solar Energy Mater. Solar Cells **78,** 143-180 (2003).

11. D. Staebler and C. R. Wronski, "Optically induced conductivity changes in discharge-produced hydrogenated amorphous silicon," J. Appl. Phys. **51,** 3262-3268 (1980).

12. M. Zeman, "Advanced amorphous silicon solar cell technologies," Thin Film Solar Cells 173-236 (2006).

13. T. Shimizu, "Staebler-Wronski effect in hydrogenated amorphous silicon and related alloy films," Japanese journal of applied physics **43,** 3257 (2004).

14. A. Shah, H. Schade, M. Vanecek, J. Meier, E. Vallat-Sauvain, N. Wyrsch, U. Kroll, C. Droz, and J. Bailat, "Thin-film silicon solar cell technology," Prog Photovoltaics Res Appl **12,** 113-142 (2004).

15. K. SöDERSTRöM Coupling light into thin silicon layers for high-efficiency solar cells (2013).

16. W. D. Eades and R. M. Swanson, "Calculation of surface generation and recombination velocities at the Si-SiO2 interface," J. Appl. Phys. **58,** 4267-4276 (1985).

17. F. Chen and L. Wang, *Light Trapping Design in Silicon-Based Solar Cells* (INTECH Open Access Publisher, 2011).

18. Anonymous https://upload.wikimedia.org/wikipedia/commons/8/8c/Optical-coating-2.png.

19. W. Ho, S. Su, Y. Lee, H. Syu, and C. Lin, "Performance-Enhanced Textured Silicon Solar Cells Based on Plasmonic Light Scattering Using Silver and Indium Nanoparticles," Materials **8,** 6668-6676 (2015).

20. Y. Wang, L. Yang, Y. Liu, Z. Mei, W. Chen, J. Li, H. Liang, A. Kuznetsov, and D. Xiaolong, "Maskless inverted pyramid texturization of silicon," Scientific reports **5,** (2015).

21. J. Zhao, A. Wang, and M. A. Green, "24· 5% Efficiency silicon PERT cells on MCZ substrates and 24· 7% efficiency PERL cells on FZ substrates," Prog Photovoltaics Res Appl **7,** 471-474 (1999).

22. M. Boccard, T. Soderstrom, P. Cuony, C. Battaglia, S. Hanni, S. Nicolay, L. Ding, M. Benkhaira, G. Bugnon, and A. Billet, "Optimization of ZnO front electrodes for high-efficiency micromorph thin-film Si solar cells," Photovoltaics, IEEE Journal of **2,** 229-235 (2012).

23. C. Das, A. Lambertz, J. Huepkes, W. Reetz, and F. Finger, "A constructive combination of antireflection and intermediate-reflector layers for a-Si/c-Si thin film solar cells," Appl. Phys. Lett. **92,** 1-053509 (2008).

24. D. Dominé, P. Buehlmann, J. Bailat, A. Billet, A. Feltrin, and C. Ballif, "Optical management in high-efficiency thin-film silicon micromorph solar cells with a silicon oxide based intermediate reflector," physica status solidi (RRL)-Rapid Research Letters **2,** 163-165 (2008).

25. B. Lipovšek, J. Krč, O. Isabella, M. Zeman, and M. Topič, "Modeling and optimization of white paint back reflectors for thin-film silicon solar cells," J. Appl. Phys. **108,** 103115 (2010).

26. L. Zeng, P. Bermel, Y. Yi, B. Alamariu, K. Broderick, J. Liu, C. Hong, X. Duan, J. Joannopoulos, and L. Kimerling, "Demonstration of enhanced absorption in thin film Si solar cells with textured photonic crystal back reflector," Appl. Phys. Lett. **93,** 221105 (2008).

27. D. Kim, I. Yun, and H. Kim, "Fabrication of rough Al doped ZnO films deposited by low pressure chemical vapor deposition for high efficiency thin film solar cells," Current Applied Physics **10,** S459-S462 (2010).

28. F. Haug and C. Ballif, "Light management in thin film silicon solar cells," Energy & Environmental Science **8,** 824-837 (2015).

29. L. Ding, M. Benkhaira, S. Nicolay, and C. Ballif,"Enhanced mobility of hydrogenated MO-LPCVD ZnO contacts for high performances thin film silicon solar cells" in *MRS Proceedings*Anonymous (Cambridge Univ Press, 2012).

30. L. Ding, M. Boccard, G. Bugnon, M. Benkhaira, S. Nicolay, M. Despeisse, F. Meillaud, and C. Ballif, "Highly transparent ZnO bilayers by LP-MOCVD as front electrodes for thin-film micromorph silicon solar cells," Solar Energy Mater. Solar Cells **98,** 331-336 (2012).

31. L. Ding, M. Boccard, G. Bugnon, M. Benkhaira, M. Despeisse, F. Sculati-Meillaud, S. Nicolay, P. Losio, O. Kluth, and P. Carroy, "New generation transparent LPCVD ZnO electrodes for enhanced photocurrent in micromorph solar cells and modules," Photovoltaics, IEEE Journal of **2,** 88-93 (2012).

32. M. Boccard, C. Battaglia, S. Hänni, K. Söderström, J. Escarré, S. Nicolay, F. Meillaud, M. Despeisse, and C. Ballif, "Multiscale transparent electrode architecture for efficient light management and carrier collection in solar cells," Nano letters **12,** 1344-1348 (2012).

33. S. Nie and S. R. Emory, "Probing Single Molecules and Single Nanoparticles by Surface-Enhanced Raman Scattering," Science **275,** 1102-1106 (1997).

34. S. A. Maier, *Plasmonics: fundamentals and applications* (Springer Science & Business Media, 2007).

35. W. Srituravanich, N. Fang, C. Sun, Q. Luo, and X. Zhang, "Plasmonic nanolithography," Nano letters **4,** 1085-1088 (2004).

36. B. Lau, M. A. Swillam, and A. S. Helmy, "Hybrid orthogonal junctions: wideband plasmonic slot-silicon waveguide couplers," Optics express **18,** 27048-27059 (2010).

37. J. Homola, "Present and future of surface plasmon resonance biosensors," Analytical and bioanalytical chemistry **377,** 528-539 (2003).

38. B. H. Nguyen, V. H. Nguyen, and D. L. Vu, "Plasmonic enhancement of light trapping into organic solar cells," Advances in Natural Sciences: Nanoscience and Nanotechnology **6,** 043002 (2015).

39. H. A. Atwater and A. Polman, "Plasmonics for improved photovoltaic devices," Nature materials **9,** 205-213 (2010).

40. M. A. Green and S. Pillai, "Harnessing plasmonics for solar cells," Nature Photonics **6,** 130-132 (2012).

41. M. Boccard, C. Battaglia, N. Blondiaux, R. Pugin, M. Despeisse, and C. Ballif, "Smoothening intermediate reflecting layer for tandem thin-film silicon solar cells," Solar Energy Mater. Solar Cells **119,** 12-17 (2013).

42. A. Hoffmann, U. Paetzhold, T. Merdzhanova, A. Lambertz, O. Höhn, C. Ulbrich, K. Bittkau, and U. Rau,"Spectrally selective intermediate reflectors for tandem thin-film silicon solar cells" in *SPIE Solar Energy Technology*Anonymous (International Society for Optics and Photonics, 2013).

43. P. O'Brien, A. Chutinan, K. Leong, N. Kherani, G. Ozin, and S. Zukotynski, "Photonic crystal intermediate reflectors for micromorph solar cells: a comparative study," Optics express **18,** 4478-4490 (2010).

44. D. Dominé, J. Steinhauser, L. Feitknecht, A. Shah, and C. Ballif, "Effect of ZnO layer as intermediate reflector in micromorph solar cells," Proc.IEEE Photovolt.Ener.Conv **3,** 1465-1468 (2006).

45. K. Peng and S. Lee, "Silicon nanowires for photovoltaic solar energy conversion," Adv Mater **23,** 198-215 (2011).

46. S. A. Razek, M. A. Swillam, and N. K. Allam, "Vertically aligned crystalline silicon nanowires with controlled diameters for energy conversion applications: Experimental and theoretical insights," J. Appl. Phys. **115,** 194305 (2014).

47. K. S. Yee, "Numerical solution of initial boundary value problems involving Maxwell's equations in isotropic media," IEEE Trans.Antennas Propag **14,** 302-307 (1966).

48. Anonymous "Lumerical Solutions, Inc." https://www.lumerical.com/tcad-products/fdtd/.

49. M. Zeman and J. Krc, "Optical and electrical modeling of thin-film silicon solar cells," J. Mater. Res. **23,** 889-898 (2008).

50. Anonymous "Synopsys TCAD," http://www.synopsys.com/tools/tcad/Pages/default.aspx.

51. A. Shah, *Thin-film silicon solar cells* (EPFL press, 2010).

52. J. Poortmans and V. Arkhipov, *Thin film solar cells: fabrication, characterization and applications* (John Wiley & Sons, 2006).

53. Tem5psu, "schematic structure of Si atoms. ," https://upload.wikimedia.org/wikipedia/commons/thumb/4/48/A-Si_structure.jpg/300px-A-Si_structure.jpg.

54. R. E. I. Schropp and M. Zeman, *Amorphous and microcrystalline silicon solar cells: modeling, materials and device technology* (Kluwer Academic, 1998).

55. M. D. Kelzenberg, "Silicon Microwire Photovoltaics," Silicon microwire photovoltaics (2010).

56. A. E. Khalifa and M. A. Swillam,"Cheap and efficient plasmonic solar cell" in *SPIE OPTO*Anonymous (International Society for Optics and Photonics, 2014).

57. A. E. Khalifa and M. A. Swillam, "Plasmonic silicon solar cells using titanium nitride: a comparative study," Journal of Nanophotonics **8,** 084098-084098 (2014).

58. M. Cortie, J. Giddings, and A. Dowd, "Optical properties and plasmon resonances of titanium nitride nanostructures," Nanotechnology **21,** 115201 (2010).

59. G. V. Naik, J. L. Schroeder, X. Ni, A. V. Kildishev, T. D. Sands, and A. Boltasseva, "Titanium nitride as a plasmonic material for visible and near-infrared wavelengths," Optical Materials Express **2,** 478-489 (2012).

60. V. E. Ferry, M. A. Verschuuren, M. C. v. Lare, R. E. Schropp, H. A. Atwater, and A. Polman, "Optimized spatial correlations for broadband light trapping nanopatterns in high efficiency ultrathin film a-Si: H solar cells," Nano letters **11,** 4239-4245 (2011).

61. V. E. Ferry, M. A. Verschuuren, H. B. Li, R. E. Schropp, H. A. Atwater, and A. Polman, "Improved red-response in thin film a-Si: H solar cells with soft-imprinted plasmonic back reflectors," Appl. Phys. Lett. **95,** 183503-183503-3 (2009).

62. X. Ni, Z. Liu, and A. V. Kildishev, "PhotonicsDB: Optical Constants,".

63. E. D. Palik, *Handbook of Optical Constants of Solids: Index* (Access Online via Elsevier, 1998).

64. O. Isabella, S. Solntsev, D. Caratelli, and M. Zeman, "3-D optical modeling of thin-film silicon solar cells on diffraction gratings," Progress in photovoltaics **21,** 94-108 (2013).

65. S. Lim, W. Mar, P. Matheu, D. Derkacs, and E. Yu, "Photocurrent spectroscopy of optical absorption enhancement in silicon photodiodes via scattering from surface plasmon polaritons in gold nanoparticles," J. Appl. Phys. **101,** 104309-104309-7 (2007).

66. P. Spinelli, V. Ferry, J. Van de Groep, M. Van Lare, M. Verschuuren, R. Schropp, H. Atwater, and A. Polman, "Plasmonic light trapping in thin-film Si solar cells," Journal of Optics **14,** 024002 (2012).

67. Anonymous "Simulation setup | FDTD Solutions Knowledge Base,".

68. C. Rockstuhl, S. Fahr, and F. Lederer, "Absorption enhancement in solar cells by localized plasmon polaritons," J. Appl. Phys. **104,** 123102-123102-7 (2008).

69. A. P. Vasudev, J. A. Schuller, and M. L. Brongersma, "Nanophotonic light trapping with patterned transparent conductive oxides," Optics Express **20,** A385-A394 (2012).

70. O. Isabella, H. Sai, M. Kondo, and M. Zeman, "Full-wave optoelectrical modeling of optimized flattened light-scattering substrate for high efficiency thin-film silicon solar cells," Prog Photovoltaics Res Appl **22,** 671-689 (2014).

71. M. A. Green, K. Emery, Y. Hishikawa, W. Warta, and E. D. Dunlop, "Solar cell efficiency tables (Version 45)," Prog Photovoltaics Res Appl **23,** 1-9 (2015).

72. D. Zhang, W. Ren, Z. Zhu, H. Zhang, B. Liu, W. Shi, X. Qin, and C. Cheng, "Highly-ordered silicon inverted nanocone arrays with broadband light antireflectance," Nanoscale research letters **10,** 1-6 (2015).

73. J. Oh, H. Yuan, and H. M. Branz, "An 18.2%-efficient black-silicon solar cell achieved through control of carrier recombination in nanostructures," Nature nanotechnology **7,** 743-748 (2012).

74. M. Dawood, T. Liew, P. Lianto, M. Hong, S. Tripathy, J. Thong, and W. Choi, "Interference lithographically defined and catalytically etched, large-area silicon nanocones from nanowires," Nanotechnology **21,** 205305 (2010).

LIST OF PUBLICATIONS

Khalifa, A. E. and Swillam, M. A., "Cheap and efficient plasmonic solar cell," SPIE OPTO, 89811R-89811R-6 (2014).

Khalifa, A. E. and Swillam, M. A. , "Plasmonic silicon solar cells using titanium nitride: a comparative study," Journal of Nanophotonics 8(1), 084098-084098 (2014).

Khalifa, A. E. and Swillam, M. A., "Silicon solar cell using optimized intermediate reflector layer," SPIE OPTO, 97430K-97430K-6 (2016).

Gouda, A.M, Khalifa, A. E., M. Elsayed, Ismail, Y and Swillam, M. A., "Self-cleaning Wideband Antireflective Silicon Nanocones for Solar Cell Applications" Presented in Photonics North Conference 2016.

Gouda, A.M, Khalifa, A. E., M. Elsayed, Ismail, Y and Swillam, M. A., “Lithography-free Wide-Angle Antireflective Self-cleaning Silicon Nanocones “ accepted with minor modifications from Optics Letter.